

# Tuneable Carbon Magnets



Sean Stansill  
University of Leeds  
School of Physics and Astronomy

Submitted in accordance with the requirements for the degree of

*Master of Physics*

May, 2019

## **Intellectual Property Statement**

The candidate confirms that the work submitted is his own and that appropriate credit has been given where reference has been made to the work of others.

This copy has been supplied on the understanding that it is copyright material and that no quotation from the thesis may be published without proper acknowledgement.

The right of Sean Stansill to be identified as Author of this work has been asserted by him in accordance with the Copyright, Designs and Patents Act 1988.

Signed : \_\_\_\_\_ Date\_\_\_\_\_

Sean Stansill

© 2019 The University of Leeds and Sean Stansill.

## Acknowledgements

First, I would like to thank my supervisor *Oscar Céspedes* who made this challenging and exciting project possible, and for giving me the creative freedom and academic insight to push myself and the brief of this project. I would also like to thank my colleagues *Shoug Alghamdi*, *Caitlin Probert* and *Ben Steele* for keeping me sane throughout this process, and for making the physics exciting.

I would like to wish a special thanks to members of the research group that have helped me along the way. Namely, everyone's hero and experimental genius *Mannan Ali*, the ever hard-working *Ruaraidh MacInnes* and to *Joseph Barker* for helping with all of my Mumax woes. As well as the rest of the academic staff whose guidance and support have make this project possible.

I cannot appreciate enough, the scientific insight of my long-time friend *Cameron Calcluth*, without whom, I would not be the physicist I am today. And, most importantly, I would like to thank *Victoria Wright* for her never-ending patience and support, and encouragement from the sidelines which has enabled me to be the person I am today.

## Abstract

The emergent properties of hybrid magnetic Co/C<sub>60</sub> bilayers is investigated as a possible replacement for rare earth magnets. Inorganic/organic phenomena have been investigated to gain a better understanding of this system, and to test the viability of a ferromagnet/molecule structure for new permanent magnet materials through magnetometry, x-ray characterisation and micromagnetic simulations.

Spin transfer from a metal to the organic produces enhanced coercivity in field cooled ferromagnet/C<sub>60</sub> films which has been shown to arise due to combination of ferromagnetic exchange coupling and exchange bias with a training mechanism unique to organic systems. In this report, coercivities of up to 0.9T and exchange bias of up to 330mT have been observed in a Co/C<sub>60</sub> bilayer. The reduction of this effect has also been observed in Co/C<sub>70</sub> which is attributed to a smaller energy barrier between C<sub>70</sub> adsorption geometries.

# CONTENTS

<b>1</b>	<b>Introduction</b>	<b>1</b>
1.1	Permanent Magnets . . . . .	2
1.2	Organic Magnets and C <sub>60</sub> . . . . .	3
<b>2</b>	<b>Theoretical Background</b>	<b>6</b>
2.1	Hysteresis . . . . .	7
2.2	Anisotropy . . . . .	8
2.2.1	Magnetocrystalline Anisotropy . . . . .	9
2.2.2	Shape Anisotropy . . . . .	10
2.3	Exchange Springs . . . . .	12
2.4	Exchange Bias . . . . .	13
2.5	Organic Hybridisation and Switching Mechanisms . . . . .	15
<b>3</b>	<b>Methodology</b>	<b>18</b>
3.1	Fabrication . . . . .	19
3.2	Magnetometry . . . . .	23
3.3	X-Ray Reflectometry . . . . .	26
<b>4</b>	<b>Characterisation of Co/C<sub>60</sub> Bilayers</b>	<b>28</b>
4.1	Enhanced pinning in Co/C <sub>60</sub> . . . . .	29
4.2	Temperature Dependent VSM . . . . .	30
4.3	Thickness Dependent VSM . . . . .	32
4.4	C <sub>70</sub> Fullerene . . . . .	34
4.5	Surface Roughness . . . . .	36
4.6	Micromagnetic Modelling . . . . .	37

## **CONTENTS**

---

<b>5 Conclusion</b>	<b>43</b>
<b>Appendices</b>	<b>46</b>
<b>A Properties of Magnetic Materials</b>	<b>47</b>
<b>B Co/C<sub>60</sub> Bilayers</b>	<b>54</b>
<b>C Mumax3</b>	<b>61</b>
<b>References</b>	<b>65</b>

## Abbreviations

AFM	Antiferromagnet	BCC	Body Centred Cubic
DFT	Density Functional Theory	DOS	Density of States
EB	Exchange Bias	EMF	Electromotive Force
FC	Field Cooled	FCC	Face Centred Cubic
FM	Ferromagnet	GMR	Giant Magnetoresistance
HCP	Hexagonal Close Packed	LHe	Liquid Helium
LLG	Landau Lifshitz Gilbert	LN <sub>2</sub>	Liquid Nitrogen
MOF	Metal Organic Framework	MR	Magnetoresistance
PEEK	Polyether Ether Ketone	PMA	Perpendicular Magnetic Anisotropy
PTFE	Polytetrafluoroethylene	PVD	Physical Vapour Deposition
RC	Resistance-Capacitor	RE	Rare Earth
RGA	Residual Gas Analyser	SC	Simple Cubic
SOC	Spin-Orbit Coupling	SOI	Spin-Orbit Interaction
UV	Ultra-Violet	VSM	Vibrating Sample Magnetometer
VTI	Variable Temperature Insert	XMCD	X-Ray Magnetic Circular Dichroism
ZFC	Zero-Field Cooled		

---

# CHAPTER 1

---

Introduction

## 1.1 Permanent Magnets

In the past few decades there has been a large increase in demand for permanent magnets: energy generation, magnetic memories (HDD, MRAM) and electric motors for environmentally friendly transportation with prominent figures such as Tesla now using permanent magnets in their electric motors [1]. Currently, the most versatile magnets produced commercially are NdFeB magnets which were first discovered in 1984 [2, 3]. This family of RE magnets has been optimised to produce a very square hysteresis loop with a large coercivity and magnetisation [4] (see Figure 1.1). And, has a Curie temperature above 300°C [5]. This combination of properties is required for a versatile, high performance permanent magnet. The large coercivity allows a magnet to be used in energy generation for many years, while a soft magnet would be quickly demagnetised by the stray field from generated currents [6]. The large magnetisation produces light, compact magnets with a large stray field. And, a high Curie temperature is useful for aerospace and electronics applications where temperature fluctuates dramatically. A high Curie temperature implies the magnet is stable and will not demagnetise, even after long-term use. The energy product  $(BH)_{max}$  is often used as a performance measure for permanent magnets that is independent of the volume of a given magnet. This is measured as half the product of the remanent magnetic flux density and coercive field (see equation 1.1) and is equal to twice the energy stored in the stray field of the magnet. NdFeB magnets have a minimum value of 300 kJ/m<sup>3</sup> [2] (see Figure A.1).

$$(BH)_{max} = \frac{B_r H_c}{2} \quad (1.1)$$

Since the development of RE magnets, there have been no new magnetic materials for permanent magnet applications which is staving off innovation. These magnets are also subject to geopolitical tensions as China produces 80% of the world's RE supply which causes large fluctuations in the cost of magnet production and insufficient global supplies [7–9]. Mining these materials requires vast amounts of energy and produces toxic effluent which is improperly disposed of [10, 11]. Thus, research has focused on using novel methods to produce magnets fabricated from cheaper, more environmentally friendly materials. We see this in many applications, for example, hard drive read heads utilize the GMR effect to increase the change in resistance between different magnetic orientations using EB to pin a reference magnetic layer in one orientation [12, 13].

Similarly, the processing of NdFeB magnets produces an exchange spring effect with Nd rich phases leading to a large uniaxial anisotropy ( $\sim 5 MJm^{-3}$  compared to  $5 kJm^{-3}$  in Fe) coupled to an Fe rich phase which has a large bulk magnetisation [14] (see Figure 1.1 and A.2). One of the most promising avenues of study, however, is that of organic materials as they are abundant, easily recyclable and have complex structures leading to electron densities of states that can't be replicated in metallic systems.

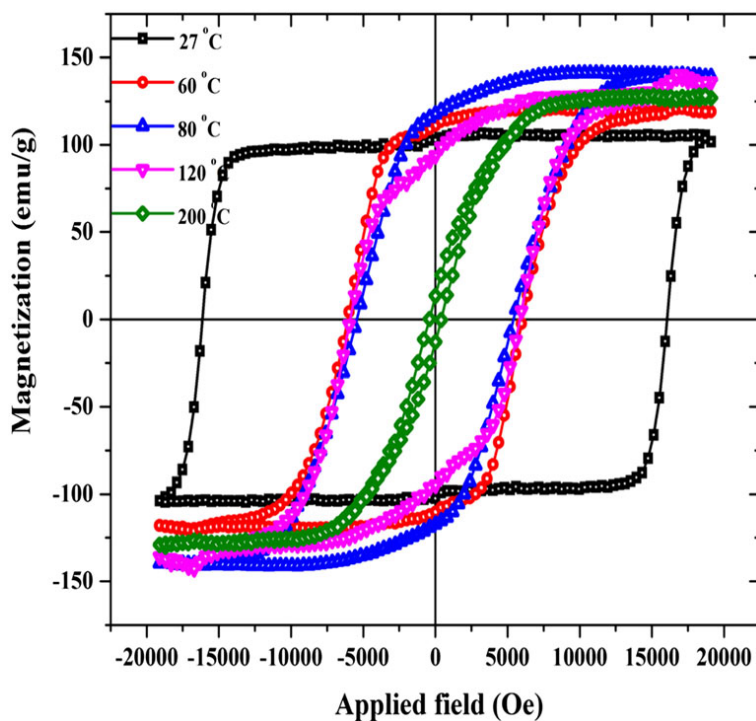


Figure 1.1: Magnetisation curves of NdFeB at various temperatures. See Table A.2 for magnetisation unit conversions. Printed from [4].

## 1.2 Organic Magnets and C<sub>60</sub>

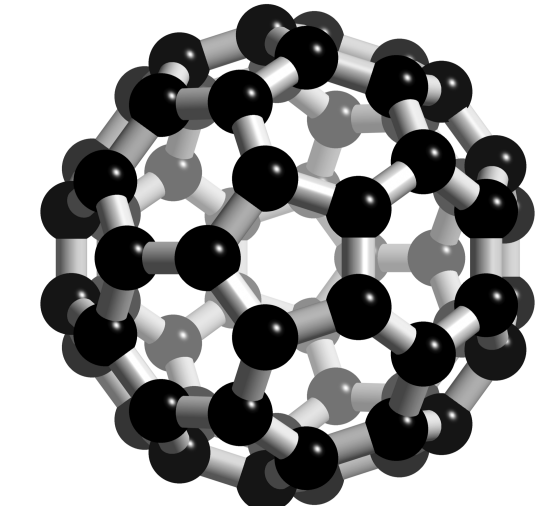
The use of organic materials in existing technologies to produce novel properties has increased over the past decade. The complex structures and mechanical flexibility of these materials has been utilized by many industries to decrease costs and increase performance of readily available products such as integrated solar cells (ie in window panes) [15], flexible OLED screens [16] and organic radio frequency identification

## 1.2 Organic Magnets and C<sub>60</sub>

---

devices (OFRIDs) [17]. The integration of organic materials into such products is a new and underdeveloped area. But, maturing technologies and cheaper production has led to an increase in research around the field of organic functional materials. Thus, the use of organics for permanent magnet applications will be explored in this report.

Since 1991, it has been shown that purely molecular systems can exhibit ferromagnetic behaviour at liquid helium temperatures [18]. Recent developments in molecular magnetism have produced single molecule magnets that have a net ferromagnetic moment at cryogenic temperatures by manipulating the DOS to overcome the Stoner Criterion [19, 20]. The difficulty with these materials is that the net magnetic moment is small, often measured as a few  $\mu_B$  per molecule, which can contain hundreds of atoms. And, spontaneous ordering usually occurs at very low temperatures [18, 20, 21]. This is much less favourable than in the naturally occurring ferromagnets which have typical values above  $1\mu_B$  per atom and have Curie temperatures hundreds of degrees above room temperature (see Table A.3 for values). However, hybridisation effects have been observed in metal/molecule systems [22–24]. In the case of *Bairagi et al* [24], this has been used to enhance PMA in Co films due to strong induced surface anisotropy attributed to the hybridisation of metal/molecule orbitals (anisotropy is discussed in Section 2.2). And, *Gruber et al* [23], has shown that long range coupling between a FM and a molecular layer can be used to tune the magnetic ordering in the organic layer, even at room temperature. This highlights progress made in manipulating the electronic structures of molecular systems to produce magnetic order. And, has led to considerable interest in hybrid metal/molecule systems, which promises to combine the recyclability and low cost of organic materials with the favourable physical properties of traditional materials for use in electronics, spintronics and permanent magnets.



© Karl Harrison 3DChem.com

Figure 1.2: Structural representation of C<sub>60</sub>. Printed from [25].

Buckminsterfullerene (C<sub>60</sub>) is an allotrope of carbon which has a near-spherical shape, high mechanical strength and high affinity to electrons (see Figure 1.2 for structure), and its discovery was awarded a Nobel prize in 1996 [26]. C<sub>60</sub> is a stable, non-toxic molecule that undergoes oxidation in oxygen rich environments via UV and visible light irradiation [27, 28]. This stability is useful for functional materials where degradation forms a vital part of producing competitive products. Along with these characteristics, it was discovered to show ferromagnetic behaviour in the Canyon Diablo meteorite: the meteorite had traces of magnetic iron but the measured magnetic moment could not be solely attributed to this contribution [29]. This discovery has led researchers to investigate C<sub>60</sub> and organic compounds (namely carbon nanotubes and MOEP [22, 30]) to produce hybrid organic ferromagnetism, despite the underlying phenomena being poorly understood. The Condensed Matter group at Leeds has studied FM/C<sub>60</sub> bilayers extensively [31–34]. With Co/C<sub>60</sub> systems exhibiting coercivities above 0.5T after field cooling in an effect which has been attributed to exchange bias [31]. This project aims to characterise and increase fundamental understanding of the coupling mechanisms and origins of enhanced coercivity in these systems.

---

# CHAPTER 2

---

Theoretical Background

## 2.1 Hysteresis

Magnetic hysteresis is a phenomenon that occurs in ferromagnets. The exchange interaction (see Figure A.3) makes the parallel alignment of spins energetically favourable, but only occurs over distances of the order of Å (see Figure A.4). Defects in the crystal lattice and grain boundaries produce small regions of uniform magnetisation called domains. When subject to a sufficiently large magnetic field, all magnetic moments will align parallel to the applied magnetic field. This is known as saturation and has a characteristic value for the magnetisation of the sample,  $M_s$ . For a ferromagnet to change its magnetisation from saturation, work has to be done to move out of this energetically favourable state in the form of applying a magnetic field in the opposing direction. In an ideal system, this would cause the coherent rotation of domains in an elastic process which follows the analytical solution of the Stoner-Wohlfarth model [35]. This model assumes a single domain, ellipsoid magnet which is a highly idealised system and ignores inelastic processes such as domain wall formation and propagation. Thus, the Stoner-Wohlfarth model produces an instantaneous switch of magnetisation from  $+M_s$  to  $-M_s$  (see Fig 2.2 for  $0^\circ$ ). In real systems, domains are flipped at defects in the crystal lattice or grain boundaries in a process called nucleation. This occurs at lattice defects as the value of the exchange interaction at these points differs from that within the rest of a grain as it is a locally frustrated state, and couples with the applied field more strongly, or couple with other local spins less. Once a domain is nucleated, spins local to the nucleation point will couple to spins now oriented parallel to the magnetic field, and the nucleated domain will propagate throughout the rest of the magnet. The value of the applied field at which  $M$  is zero is known as the coercivity. A magnetic material with a large coercivity is known as a hard magnet and materials with a small coercivity are labelled soft. There is no rigorous definition of what value of coercivity makes a material hard or soft, but the distinction is important as these two types of materials have vastly different functions - low coercivity materials lose little energy when magnetising and demagnetising (useful for transformers). And, hard materials are used as permanent magnets. The domain structure in a magnet acts as a memory, since the response to applying a magnetic field will depend upon whether it was previously magnetised in the positive or negative direction. This produces an M/H relationship that is not one to one and is known as the hysteresis loop, which derives its name from the Latin of “to lag behind” (see Figure 2.1).

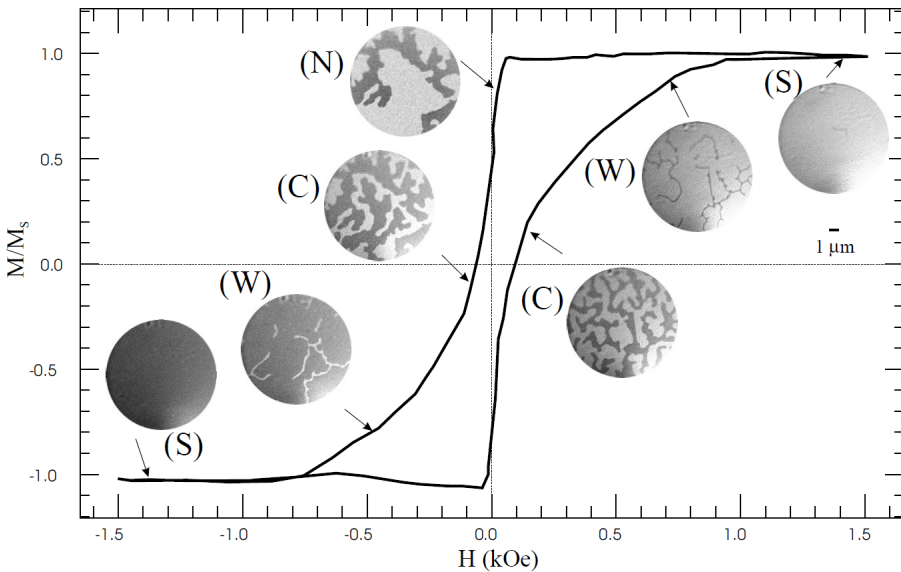


Figure 2.1: A sequence of magnetic images of a layered Gd-Fe system in a varying applied magnetic field covering the complete hysteresis loop. The different stages saturation (S), nucleation (N) and worm-like domains (W) are marked. Printed from [36].

The shape of the hysteresis loop for a given magnet is important. As discussed in Section 1.1, for permanent magnets, a square hysteresis with large saturation magnetisation and coercivity is essential. There are a range of intrinsic and extrinsic properties which determine the shape of a hysteresis loop. Some of these properties will be discussed in this chapter.

## 2.2 Anisotropy

Anisotropy is the name given to the tendency for the magnetisation to lie along a fixed axis. There are many sources of magnetic anisotropy including shape, induced and magnetocrystalline anisotropy. Shape and induced anisotropy are extrinsic properties and will vary between different samples, whereas magnetocrystalline anisotropy is an intrinsic property of a material. For the purpose of this report, only magnetocrystalline and shape anisotropy will be discussed.

### 2.2.1 Magnetocrystalline Anisotropy

Magnetocrystalline anisotropy arises due to the crystal structure of a ferromagnet, spin orbit coupling (see Figure A.5) and dipole interactions. SOC is the interaction of an electron's spin ( $S$ ) and its orbital momentum ( $L$ ) in an atomic lattice. Thus, when the direction of an electron spin changes with respect to the crystal axes, there is a change in potential energy. There is a secondary contribution for non-cubic crystal lattices due to the shape of the charge distribution in the lattice. In cubic systems (see Figure A.6a), this charge density has spherical symmetry so there are no contributions to anisotropy. Hexagonal lattices do not have a spherical distribution of charge. This produces an energy potential that is smaller along one crystallographic direction. Bulk Co has a hcp crystal structure (see Figure A.6c), so has a unique easy direction along the hexagonal [001] axis which is represented by an energy density as in Equation 2.1.  $\theta$  is the angle from the [001] easy axis,  $K_1$  is the first order anisotropy constant and  $K_2$  is the second order anisotropy constant in units of  $Jm^{-3}$ . Fe and Ni, however, have an fcc structure so  $\langle 100 \rangle$  and  $\langle 111 \rangle$  act as the easy and hard directions (see Figure A.7).

$$E = K_1 \sin^2 \theta + K_2 \sin^4 \theta \quad (2.1)$$

This leads to different hysteresis loops for each crystallographic direction. For easy axis loops, the curve appears square with a large difference between the behaviour of  $M$  for increasing and decreasing applied field  $H$  (see Figure 2.2 for  $0^\circ$ ) with a large remanent magnetisation. Whereas hard axis loops have near zero coercivity and remanent moment (see Figure 2.2 for  $90^\circ$ ).

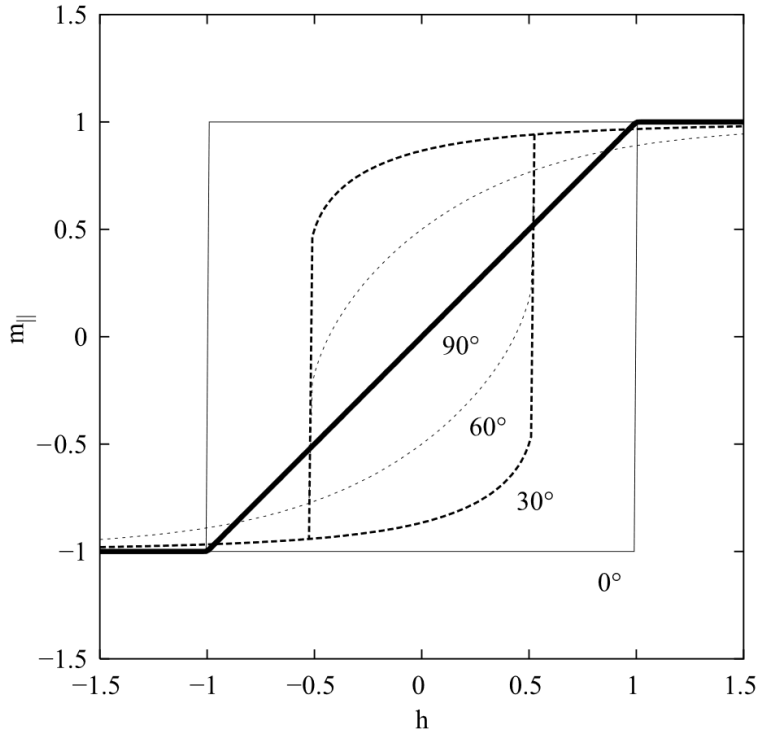


Figure 2.2: Magnetisation solutions of the Stoner-Wohlfarth model of single domain ferromagnets. Angles in  $^\circ$  are between the applied field  $h$  and the easy axis of the material. Printed from [37].

### 2.2.2 Shape Anisotropy

Shape anisotropy is the effect of the shape of a magnet (cuboid, ellipsoidal, etc) on its preferred direction of magnetisation. This effect arises due to the size of the demagnetising field which opposes the magnetisation for a given geometry. And, this phenomenon is why the magnetisation of a ferromagnet tends towards zero when left in zero applied field for a long period of time. Consider equations 2.2 and 2.3, the definition of magnetic flux density and Gauss's law for magnetism. Inside a magnetic material, these equations must also hold. By taking the divergence of Eq 2.2 and substituting into Eq 2.3, we expect Eq 2.4 to be true. In fact,  $H$  has two contributions. For  $H$  residing within the magnet, this is known as the demagnetising field. And, for the component outside the magnet, this is known as the stray field (see Figure A.8).

$$B = \mu_0(M + H) \quad (2.2)$$

## 2.2 Anisotropy

---

$$\nabla \cdot B = 0 \quad (2.3)$$

$$\nabla \cdot H = -\nabla \cdot M \quad (2.4)$$

The demagnetising field is usually not uniform inside a given geometry. In fact, only in an ellipsoid with a specific ratio of major and minor axes is this demagnetising field uniform. Thus, different shaped magnets have a different amount of energy stored in its stray field, which is given by Eq 2.5 [38]. This can be simplified for specific geometries (and is often approximated for non-uniform shapes) through the use of a demagnetisation factor,  $D$ , which is given in Eq 2.6, assuming the direction of  $M$  lies along the axis with demag factor  $D$ . This has led to many commercially available magnets to be produced in squat cylinders as these have demagnetisation factors of 1/2 for the radial direction and 0 for the z direction. This leads  $M$  lying preferentially along the z direction, increasing the longevity of the permanent magnet while increasing the value of the stray field. This project works with thin films which have demagnetisation factors of 0 parallel to the plane of the film and 1 perpendicular to the film which causes  $M$  to lie preferentially along the plane of the film.

$$\epsilon_m = -\frac{1}{2}\mu_0 \int_{sample} H \cdot M dV \quad (2.5)$$

$$\epsilon_m = \frac{1}{2}\mu_0 V D M_s^2 \quad (2.6)$$

However, for extremely thin samples, the magnetisation of thin films can tend to lie perpendicular to the film due to surface or magnetocrystalline anisotropy. This occurs when a highly oriented thin film is grown such that its easy axis lies perpendicular to the film. Or, when films are thin enough (one or two atomic layers), surface effects pull the anisotropy out of plane [39]. This is known as perpendicular magnetic anisotropy and is commonly used in magnetic storage devices, as longitudinal methods have a limited achievable areal density due to the superparamagnetic limit [40]. Thus, the development of permanent magnetis with large PMA is desirable for commercial use.

## 2.3 Exchange Springs

An exchange spring system is one in which there are two magnetic materials deposited in a repeating bilayer structure; one magnetically hard material, and one soft [41]. This process combines the large coercivity of the hard material and the large magnetisation of the soft material (see Figure 2.3). This occurs since the soft layer, which is sandwiched between two hard layers, will be pinned when in a negative magnetic field by the hard material through interlayer exchange coupling. Thus, the soft layer will remain magnetised in a given direction until the hard material switches magnetisation. This effect is smaller in bilayer systems as there is only one interface at which interlayer exchange coupling occurs [42]. Instead of complete pinning of the soft layer, the soft layer will begin magnetisation reversal [43]. This forms a region, perpendicular to the plane of the bilayer film, in which the magnetic moments rotate in either a Bloch or Néel configuration (see Figure A.9). This is because a large discontinuity in  $M$  has a larger energy cost than a small switching region, even in dimensionally constrained thin films. This still has the effect of increasing the coercivity of the soft material, but to a lesser extent than multilayer systems. Often this appears as a hysteresis loop with two distinct phases (see Figure A.10). This also produces a larger reversible portion of the hysteresis loop. If the soft layer has begun switching and the magnetic field is removed, the hard layer will exert a magnetic torque on the soft layer, which will return to near saturation [44]. This ‘springing’ action led to this phenomenon to be called an exchange spring.

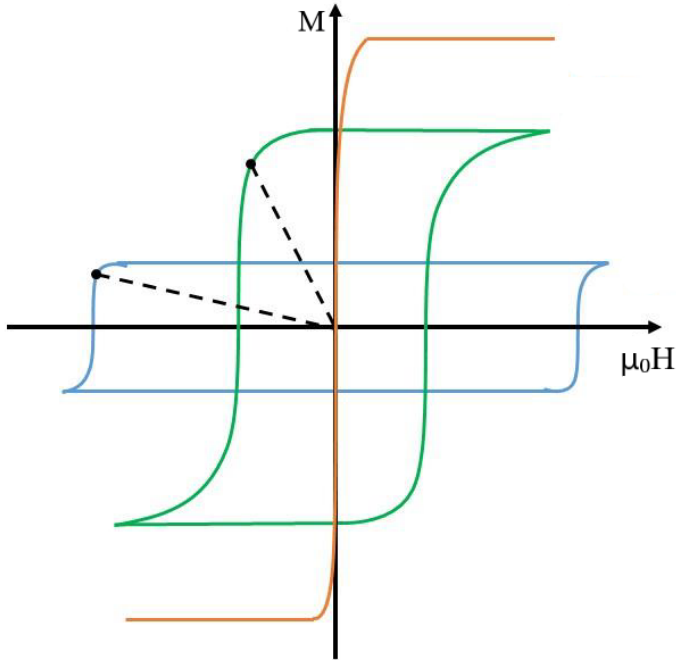


Figure 2.3: Schematic hysteresis curves of a soft magnet (orange), hard magnet (blue) and an ideal multilayer exchange spring (green). The energy product is represented by the black dot, which has a larger value for the exchange spring magnet. Adapted from [45].

This effect was used in early magnetic recording media to produce non-volatile magnetisation states that represented bits [46, 47], and is a common tool in the processing of permanent magnets to increase their coercivity.

## 2.4 Exchange Bias

Antiferromagnetism occurs when the exchange constant,  $\mathcal{J}$ , is negative for a given material. This causes spins to preferentially align in an antiparallel configuration. These materials have zero net magnetic moment and do not couple strongly with external magnetic fields (unlike paramagnetic and diamagnetic materials). These materials had no practical applications in magnetic materials until the discovery of exchange bias - despite this being a highly ordered magnetic system. In 1956, a new type of magnetic anisotropy was discovered, unique in that it acts unidirectionally instead of uniaxially, as with magnetocrystalline anisotropy [48, 49]. The hysteresis curves for Co micro-

## 2.4 Exchange Bias

---

particles with a CoO shell exhibited an increase in coercivity and a horizontal translation (known as exchange bias, see Figure A.11), dependent on whether or not the sample was cooled below the Néel temperature in a saturating magnetic field. This anisotropy was measured to be of the same order of magnitude as the magnetocrystalline anisotropy of Co, making this an important tool to produce a pinned system which remains near positive saturation indefinitely. Exchange anisotropy occurs due to the pinning of a ferromagnetic layer to an antiferromagnet across an interface [50]. When at a temperature higher than the Néel temperature, the AFM is disordered, much like a FM above the Curie temperature. When cooled from between the Néel and Curie temperatures to below the Néel temperature in a saturating magnetic field, the ferromagnet applies an effective field on interfacial AFM atoms, producing symmetry breaking and causing AFM domain formation that is coupled with the FM domains. This introduces an additional energy term which must be overcome to switch the direction of magnetisation. The choice of which direction the cooling field is applied is commonly known as setting the exchange bias, since the direction of the applied field will determine the preferred magnetisation direction of the exchange biased system. If the exchange interaction between the FM and AFM is sufficiently strong across the interface, then it is possible to produce a system that is always saturated in zero applied field (see Fig 4.9). This possibility has led to the production of spin-valves which utilise EB and GMR for use as magnetic field sensors or magnetic memory read heads.

Antiferromagnets with Néel temperatures much higher than room temperature produce EB systems that can be used as permanent magnets, due to the always saturated remanence, providing versatile permanent magnets [12, 52]. The pinning of an FM/AFM bilayer can be reduced by multiple iterations of a field sweep. This reduces the number of interacting interfacial spins in an effect known as training [53]. Cooling in field produces many, small domains in the AFM which correspond with the grains in the FM due to interlayer exchange coupling. Demagnetising and remagnetising the ferromagnetic layer causes domain wall propagation in the AFM producing a system with a random domain structure in the AFM - similar to oscillating a magnetic field about 0 to produce a virgin state in a FM. It often takes many iterations to destroy all exchange bias, as in [54], twenty loops are required to show agreement with the hysteresis of zero-field cooled samples. Although, there are two contributions to the

## 2.5 Organic Hybridisation and Switching Mechanisms

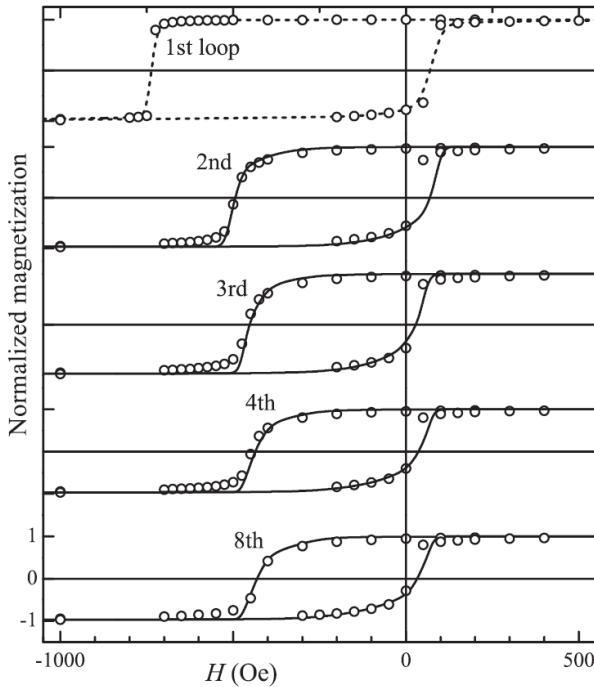


Figure 2.4: Hysteresis loops of field cooled Co/CoO bilayers at 10K showing the training effect between subsequent loops. Symbols represent experimental data, whereas the curves are simulated. Printed from [51].

training effect: athermal and thermal training. The training method described above for number of field sweeps  $n > 1$ , is attributed to thermal fluctuations randomly changing domain structures within the AFM and intergrain exchange coupling [55]. Some systems have very weak intergrain exchange coupling so the only training effect observed is for the  $n = 1$  sweep. This is the athermal training effect and is the largest source of training - up to 80% of the increase in  $H_c$  can be destroyed in the first sweep for typical AFMs [55]. This is attributed to the irreversible switching of AFM domains when the FM undergoes reversal (see Figure 2.4).

## 2.5 Organic Hybridisation and Switching Mechanisms

In metals, the electron DOS consists of a band structure which, for the room temperature ferromagnets Fe, Co and Ni, is split between spin-up and spin-down orientations at the Fermi level (see Figure A.12). This leads to an energetically favourable state in

## 2.5 Organic Hybridisation and Switching Mechanisms

which local spins align parallel, and becomes disordered above the critical Curie temperature ( $T_C$ ) at which point thermal fluctuations destroy magnetic order. It has been shown in hybrid metal/organic systems that it is possible to produce ferromagnetism in paramagnetic Cu via interfacial hybridisation with C<sub>60</sub> [33]. When well separated from a metal, molecules have discrete energy levels. But, in close proximity (ie in a bilayer system) the *s* orbital of the organic molecule and 3*d* orbital of the metal produce a hybrid state in which there is an overlap of these orbitals (see Figure 2.5). This produces a weak, spin polarised band structure in the organic layer which leads to magnetic behaviour that can be either ferromagnetic or antiferromagnetic. More accurately, there is spin-polarised transfer of electrons from the metal to the organic layer due to the large electronegativity of the C<sub>60</sub> and natural spin order in the ferromagnet. If this coupling is antiferromagnetic then a suppression of magnetic moment in the sample is observed and has been reported in Co/C<sub>60</sub> bilayers [31].

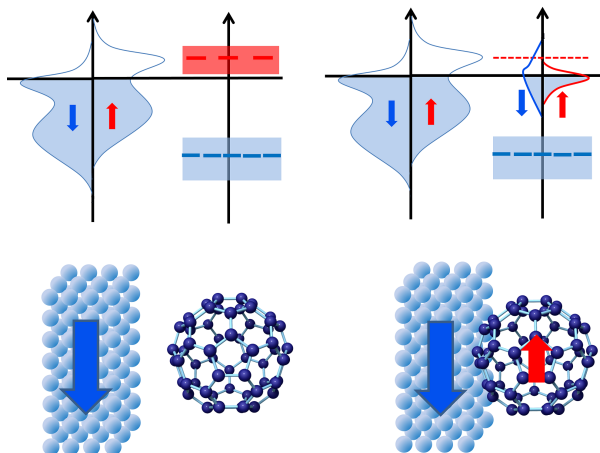


Figure 2.5: Hybridisation of Co and C<sub>60</sub> density of states when well separated (left, blue level is the HOMO and the red level is the LUMO) and in close proximity (right). Printed from [32].

C<sub>60</sub> has two crystalline phases. At room temperature, the C<sub>60</sub> cages form an fcc lattice, but when cooled below 120K this transitions to a SC structure. Due to the spherical symmetry of C<sub>60</sub>, the cages can freely rotate between lying on a carbon hexagon-hexagon (HH), pentagon-pentagon (PP) or hexagon-pentagon (HP) bond, or a hexagon (H) or pentagon (P) face, which have an energy barrier between them of

## 2.5 Organic Hybridisation and Switching Mechanisms

---

the order of 0.1eV per cage (see Table B.1). When cooled further, to below 90K, energy from thermal fluctuations is smaller than the energy between these different states - thermal energy of one  $C_{60}$  cage is approximately 0.2eV at this temperature (60 carbon atoms with  $\frac{1}{2}k_B T$  energy) which corresponds to the energy barrier for the transition from a HP to HH geometry (see Table B.1) [56, 57]. So, cages are effectively frozen into one orientation, with each orientation coupling differently to a metallic layer. DFT calculations have shown that  $C_{60}$  couples both ferromagnetically and anti-ferromagnetically to a Co layer (see Figure 2.6). And, that a HH geometry has stronger antiferromagnetic coupling due to shorter range electron transfer from Co to  $C_{60}$  than a HP geometry. This AFM coupling reduces the net magnetic moment of the system, giving a saturation magnetisation of less than the literary value of 1440emu/cc. The spin distribution within a  $C_{60}$  cage in either HP or HH geometry is asymmetric (see Table B.1). Thus, when an external magnetic field is applied, a torque is exerted on cages in these geometries which will cause switching to a more symmetric H or P state. This process causes a large enhancement of the coercivity upon the first sweep in an irreversible switching process which is of interest for permanent magnet applications (see Section 2.1).

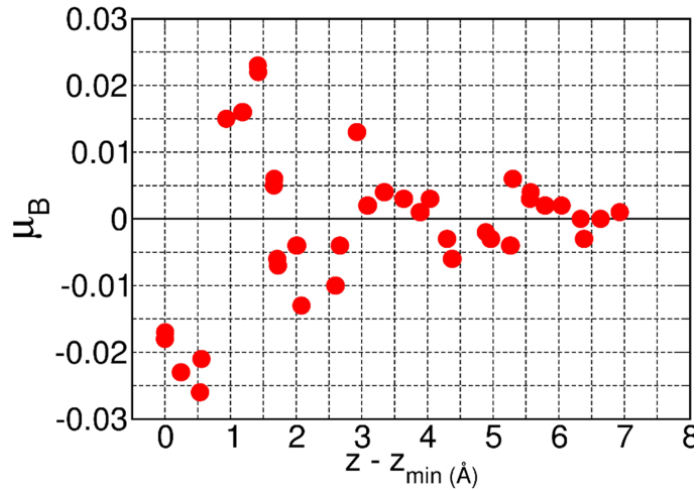


Figure 2.6: DFT calculations of the distribution of injected spins from a positively magnetised hcp cobalt layer to a  $C_{60}$  cage in a HP geometry. Printed from [31].

---

# CHAPTER 3

---

Methodology

### 3.1 Fabrication

Samples were fabricated using DC magnetron sputtering for metallic layers, and thermal evaporation for C<sub>60</sub> deposition. Samples were grown on thermally oxidised silicon substrates that were (8 × 8)mm or (4 × 4)mm in size. The substrates were cleaned using acetone in a sonicator to remove impurities from the surface. This also has the effect of degassing the substrate. Samples were then dried using compressed air to reduce the risk of dust adhesion. This process is repeated using isopropanol. as acetone leaves more residue on the surface but is a better solvent. Substrates are then attached to trapezes, ensuring that the smooth side is pointing upwards to ensure growth occurs on a homogeneous, atomically smooth surface which ensures minimal roughness of grown films. These trapezes are then loaded onto a sample wheel which is moved mechanically in the system during growth between different guns to allow multilayer structures to be produced.

Sputtering allows the production of high purity samples with a good polycrystalline structure and surface roughness of a few Å due to a highly controlled environment in which growth occurs. This is achieved by creating a high vacuum environment with the use of two pumps (see Figure 3.1). The two pump design is required to achieve a high vacuum as high vacuum pumps do not work efficiently at pressures above the order of mTorr (often this will damage a high vacuum pump). And, regular roughing pumps cannot achieve this level of vacuum. First, the system is pumped from atmospheric pressure to < 25mTorr using a mechanical roughing pump. At this pressure, the composition of residual gases which form the load on the pump is mostly water vapour (water is very stable, even under vacuum conditions), as the true gases like N<sub>2</sub> and O<sub>2</sub> are easily removed [58]. Once a rough vacuum is achieved, the roughing pump is switched off, then the cryopump is switched on. This step of switching off one pump before another is switched on is important, as the throughput of the cryopump will be much greater than that of the roughing pump. So, if this step is omitted, there would be backflow of gas and oil into the system which would both cause damage to the roughing pump and cryopump - oils would freeze on the cryopanels, reducing the effectiveness of the pump, which would have to be taken apart to be cleaned. And, the lack of a clean vacuum would render that grown cycle unusable. The cryopump works in diffuse atmospheres to condense residual gases onto plates which are kept at

### 3.1 Fabrication

temperatures below 20K. This ensures that residual gases, as well as water vapour, are condensed and removed from the atmosphere. This process can take a long time to produce a high vacuum of  $10^{-7}$  Torr, or better, due to the weak (mostly Van der Waals) forces that act on residual gas in this physical process (as opposed to chemisorption type pumps) [59]. Thus, the cryopump is left overnight to achieve a high vacuum.

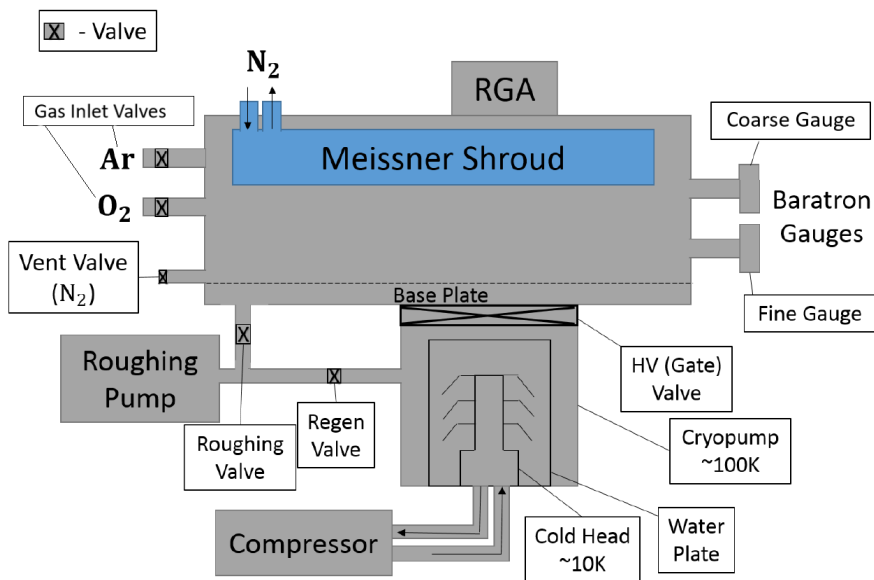


Figure 3.1: Schematic diagram of the sputter deposition system, including all relevant components. Adapted from [34].

At high vacuum, the gas pressure is low enough to use an RGA. This works in a similar process to mass spectrometry, in which gas species in the chamber are ionised and separated by their momentum. For an RGA, a high gas pressure is equivalent to a very high current through the device (movement of ionised species hitting a detector plate) which can damage the RGA, or be a health and safety risk of electrocution. So, it is only used once a high vacuum has been achieved. The system has an integrated Meissner shroud (see Figure 3.1). And, when a high vacuum is achieved, mostly  $H_2O$  remains in the chamber, which is undesirable due to the possibility of oxidation of samples (some metals are reactive and readily form oxides with water as with rusting Fe). The Meissner shroud has liquid nitrogen pumped through it for at least two hours before growth starts. This produces a large surface on which water will condense and freeze on to remove it from the vacuum. This large surface area is important as the flow

### 3.1 Fabrication

of molecules in the vacuum chamber is no longer viscous but molecular, so the removal of water is mostly affected by the fraction of the surface area which the Meissner shroud occupies. With all the above steps a vacuum of  $10^{-8}$  Torr is achievable which yields very low impurity levels in grown samples.

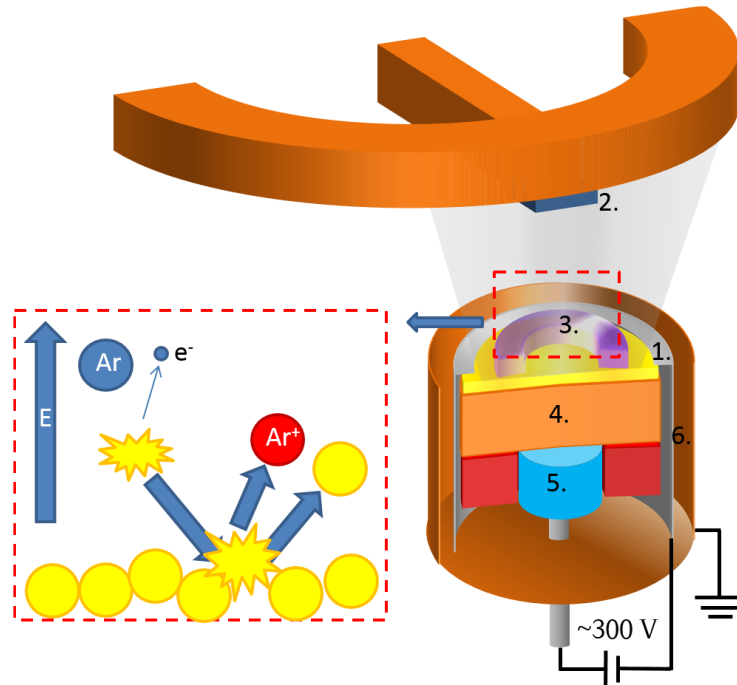


Figure 3.2: A schematic diagram of a sputter gun. Labelled sections of the diagram are: 1) the anode 2) sample substrate, onto which material will be sputtered 3) metal target which forms the cathode 4) copper spacer to prevent demagnetisation of the magnetron 5) the magnetron 6) shielding to prevent a build up of static charge. Printed from [32].

Since sputtered samples produced for this project are made from metallic materials, only DC sputtering will be discussed. Although RF, reactive and co-sputtering are used for insulating, molecular and alloyed materials respectively. From this point, *sputtering* will be used to refer to *DC sputtering*. Sputtering is a PVD method of sample fabrication which encompasses any method to produce films in which a solid target undergoes vaporisation produced via physical methods (ie evaporation or plasma formation) that is sublimated onto a substrate to produce a film. The process of sputtering uses an inert gas, usually Ar due to its large atomic mass which efficiently transfers momentum to sputtered atoms, and a large electric field applied between the target

### **3.1 Fabrication**

---

(cathode) and substrate (anode) to break down Ar into an ion and an electron which are then accelerated by the electric field and produces a plasma arc (note this potential differs dependent on the distance between electrodes and the gas considered). These initial Ar ions will collide with the cathode and impart its momentum to metal atoms which introduces more electrons to the system, sustaining the plasma arc (see Figure 3.2). This bombardment of the metal target by Ar ions results in back scattering of metal atoms, which sublimates onto the substrate, producing a thin film. The use of a magnetron produces a magnetic field shaped in a ring around the cathode such that the density of ions and electrons is increased in this region. This produces antiparallel cyclic motion of the positive ions and negative electrons by the Lorentz force, which increases the number of collisions with neutral Ar, further increasing the bombardment of the metal target. This increases the efficiency of the process and decreases growth times. To reduce oxidised phases and to degas the targets, a presputter procedure is adopted. When at high vacuum, guns are lit for 30 seconds to remove oxide layers that have formed on the high purity targets and excite gas molecules that have diffused into the targets. This improves the quality of grown films and reduces surface roughness which is vital when investigating interfacial effects. To ensure films are the correct thicknesses, voltages are used that have been calibrated by sputtering thick films of these materials which are analysed using XRR (see Section 3.3) to accurately determine the thickness which is then used, along with growth times, to calculate a deposition rate.

Both C<sub>60</sub> and C<sub>70</sub> were used in this project which follow the same deposition technique. An ampoule containing the organic material is heated in stages by applying an electric current through a tungsten filament which ensures uniform heating and degases the molecules. This reduces the risk of oxidation and decomposition into other organic compounds which are lighter and evaporate more easily. This would act as an impurity in organic films so should be avoided. The current is ramped to 21.5A which heats filament to a few hundred Kelvin. In atmospheric conditions, this would not be sufficient to sublime such large molecules, as it has been seen to occur readily at 800°C under a nitrogen atmosphere [60, 61]. But, in high vacuum conditions, sublimation occurs much more readily, and lower temperatures reduce the risk of thermal decomposition of C<sub>60</sub> [62]. The deposition rate varies between 0.1-0.3Å/s as measured by a quartz

### **3.2 Magnetometry**

---

oscillator. This measures the damping of oscillations by an increase in adsorbed mass over time. Such a low deposition rate increases the order of deposited C<sub>60</sub>, although previous work has shown this is not crystalline [32, 63], ensuring maximal interfacial effects are observed. A decrease in this rate implies that the ampoule has been emptied of organic material, whereas an increase implies that lighter organic matter is being deposited - either due to a current level that is too high, or a large amount of oxygen in the system causing the decomposition of C<sub>60</sub>. It is important to ensure Ar gas flow is switched off when organic films are being deposited as an excess in gas would cause collisions between gas molecules and C<sub>60</sub>. This increases spread of the plume of organic material, decreasing the amount of material deposited onto the substrate as compared to the quartz oscillator (the oscillator is positioned within the C<sub>60</sub> housing so collisions have minimal impact).

## **3.2 Magnetometry**

The primary method in which these magnetic samples were characterised was through the use of a VSM. A VSM uses Faraday's law (see Equation 3.1) to measure the induced potential difference in pickup coils from a vibrating magnetised sample, which oscillates at a fixed, well defined frequency (55Hz), producing a change in magnetic flux through the pickup coils ( $\frac{d\Phi}{dt}$  in Eq 3.1). This is effective, as it is much easier to measure a potential difference than to use a magnetic field sensor - electrical measurements are often more sensitive than field sensors. And, this removes the background contribution from the applied magnetic field, so magnetisation,  $M$ , is measured directly, as opposed to measuring the magnetic flux density,  $B$ , (see Eq 2.2) which would require additional processing of raw data.

$$emf = -\frac{d\Phi}{dt} \quad (3.1)$$

The magnetic field is provided by a split-pair of superconducting coils, located in a liquid helium bath. To reduce helium boil off, and reduce the risk of quenching the superconducting magnet, the cryostat has a layered structure (see Figure 3.3). This ensures the VTI and helium reservoir is very well insulated from the external environment. The use of superconducting coils allows magnetic fields up to 8T to be produced.

### 3.2 Magnetometry

The system at the University of Leeds is a VSM inside a helium flow cryostat which allows samples to be measured in a large range of temperatures ( $< 4K - 300K$ ). The temperature is controlled by balancing the flow of liquid helium (at 4.2K) and the current through a DC heat exchanger. The use of a DC heater reduces the electrical noise during measurements as only AC signals are measured. It is possible to achieve temperatures lower than the boiling point of He since the LHe is being moved from an area of high pressure (LHe reservoir) to a rough vacuum with very low pressure. This decrease in pressure reduces the temperature thermodynamically and can be well approximated using the ideal gas equation (see Figure A.13) which allows temperatures below 3K to be achieved. This requires additional consideration when operating at such low temperatures for extended periods of time as the lambda point of He is around 2.1K [64].

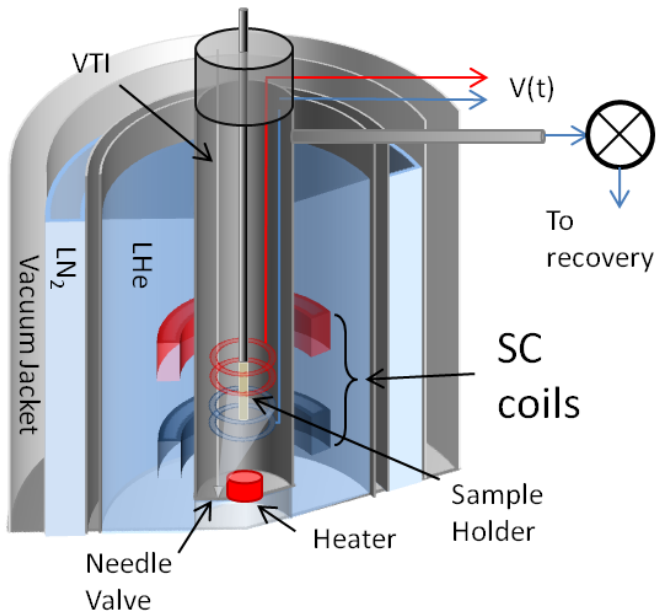


Figure 3.3: Schematic diagram of the VSM system. Printed from [32].

The sample is attached to a PEEK rod using teflon tape which is then attached to a carbon fibre rod which is specially designed to reduce noise in the oscillations by having a finely tuned resonant frequency. To ensure there are no magnetic impurities introduced, a workbench reserved for non-ferrous tools and equipment is used for

### **3.2 Magnetometry**

---

sample preparation and mounting. When loading, the VTI is overpressurised, has a temperature above 100K and helium flow is at 100%, ensuring that little atmospheric gas enters the system to reduce the risk of liquid oxygen and nitrogen formation (liquid oxygen boils at 90K) as well as reduce water vapour intake which would freeze on, and jam the needle valve used to control helium flow. After loading, the system is pumped down to a rough vacuum and a small helium flow is passed through the VTI to ensure a uniform temperature is maintained throughout. Before taking measurements, the sample has to be centred. This ensures that the sample is subject to the full magnetic flux which corresponds to the value assumed by the software. And, so that the pickup coils are measuring the whole signal from the magnetised sample. This z-centring process must be done in the presence of a small magnetic field (around 0.05T) to ensure the sample is magnetised and to measure the diamagnetic signal of sample substrate. This produces a well defined spectrum when measuring the absolute electrical signal against z which has a three peak form; two minor peaks between a major peak (see Figure 3.4). The two minor peaks correspond to the diamagnetic component from the sample substrate (although the PEEK sample stick and PTFE tape contribute, this is smaller than the specific susceptibility of SiO<sub>2</sub> [65]), with the major peak corresponding to the ferromagnetic sample (note minor peaks have a negative signal but the software plots absolute values).

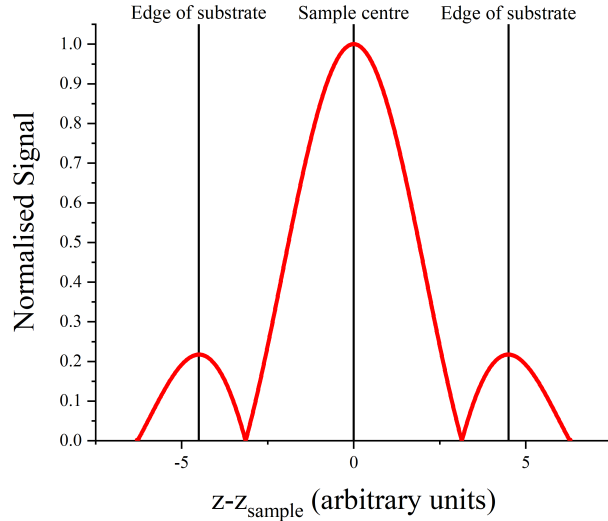


Figure 3.4: Example of an ideal  $z$  centring curve for a ferromagnetic sample in a VSM.

### 3.3 X-Ray Reflectometry

XRR was used to structurally characterise calibration samples of Ta to probe surface roughness and sample thickness. The advantage of using x-rays is that this is a non-destructive method to probe atomic scale structural characteristics of a sample. The experimental technique of XRR is built on a simple concept: collimated x-rays are shone onto a smooth surface of a known element at a small variable angle and the number of x-ray photons reflected specularly are measured.

$$n_1 \sin \theta_1 = n_2 \sin \theta_2 \quad (3.2)$$

$$n\lambda = 2d \sin \theta \quad (3.3)$$

For metals, the refractive index,  $n$ , experienced by x-rays is less than one (the approximate value of the refractive index of air). Thus, by Snell's law (Eq 3.2), there exists some critical angle that total external reflection occurs (similar to total internal reflection but for materials with  $n < 1$ ) [66]. This is why, in Fig 3.5 for small angles, we see an increase in intensity, up to a critical angle. After this critical angle, fringes are observed, which are dependent on the thickness of the film being measured. Reflection

### 3.3 X-Ray Reflectometry

occurs due to Bragg's law (see Eq 3.3) when the photon wavelength is similar to the atomic spacing of the material, an interference pattern is produced. Each atomic layer in the sample being measured contributes to these fringes. Reflected photons from different layers have a small phase difference which produces constructive and destructive interference for specific values of  $\theta$ , with constructive interference fringes determined by Bragg's law. So, in highly amorphous samples (no crystal structure) it is expected that these fringes are barely discernible and that the signal drops off quickly with increasing angle due to a large portion of diffuse reflection. In crystalline samples, these fringes - known as Keissig fringes - are very clear. The distance between adjacent fringes is related to the sample's thickness by Eq 3.4 where  $\theta_c$  is the critical angle,  $n$  is the Keissig fringe number,  $\lambda$  is the wavelength of light and  $t$  is the sample thickness. The effect of surface roughness is to increase the amount of diffuse reflection of reflected photons. This increases the drop-off rate of the overall intensity.

$$\theta^2 - \theta_c^2 = n^2 \left( \frac{\lambda}{2t} \right)^2 \quad (3.4)$$

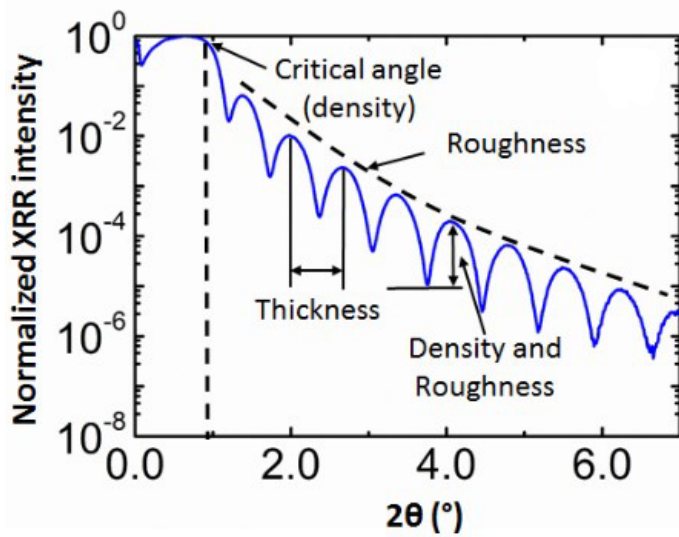


Figure 3.5: XRR curve highlighting the effect sample thickness, roughness and density on an XRR curve. Printed from [67].

---

# CHAPTER 4

---

Characterisation of Co/C<sub>60</sub> Bilayers

## 4.1 Enhanced pinning in Co/C<sub>60</sub>

Initial work with samples Co/C<sub>60</sub> bilayers was to verify that field cooled samples exhibited pinning when cooled in a saturating magnetic field (see Figure 4.1). To ensure surface roughness was constrained to a few Å, and that samples had a good polycrystalline structure grown in a known direction, a seed layer of Ta was used. This non-magnetic element grows, as deposited, as a bcc lattice [68] (see Figure A.6b) which promotes deposited Co layers to grow in a similar structure. This structure has a higher surface packing density than hcp which increases the points of contact between Co and C<sub>60</sub>, which in turn increases the effective interlayer exchange coupling. An Al capping layer was used to prevent C<sub>60</sub> oxidation. This was 8nm thick, much larger than the thickness of usual capping layers, as oxygen penetration forms an alumina layer up to 4nm thick [69]. The deposition of Al directly onto C<sub>60</sub> produces clustering, and an uneven distribution in thinner Al layers. Some samples showed no pinning, despite being in the same growth cycle under the same conditions as the sample pictured below. This is attributed to a failed interface in which interfacial coupling is negligible, although this has not been confirmed experimentally. In addition, samples which exhibit no pinning also show a very small coercivity ( $\sim$  Oe) as compared with samples of similar composition, which confirms an exchange spring effect when spin-polarised electron transfer is present (see Figures B.1 and 4.1 (red curve)). This implies that the anisotropy of C<sub>60</sub> cages which exhibit this behaviour is much greater than that of a deposited bare Co film. This increase in coercivity is observed at temperatures much higher than the blocking temperature of field cooled samples - up to 120K has been measured, although  $H_c(T)$  has not been measured in ZFC samples. This suggests the effective Curie temperature of C<sub>60</sub> cages is greater than the effective Néel temperature of around 94K. The raw data is given as a magnetic moment so, to calculate a magnetisation, the area of the sample was measured and the thickness considered was that of the Co layer, not the entire stack. Thus, any variations from 1440emu/cc is due to AFM coupling of C<sub>60</sub> quenching of the net moment (similar to a ferrimagnet).

## 4.2 Temperature Dependent VSM

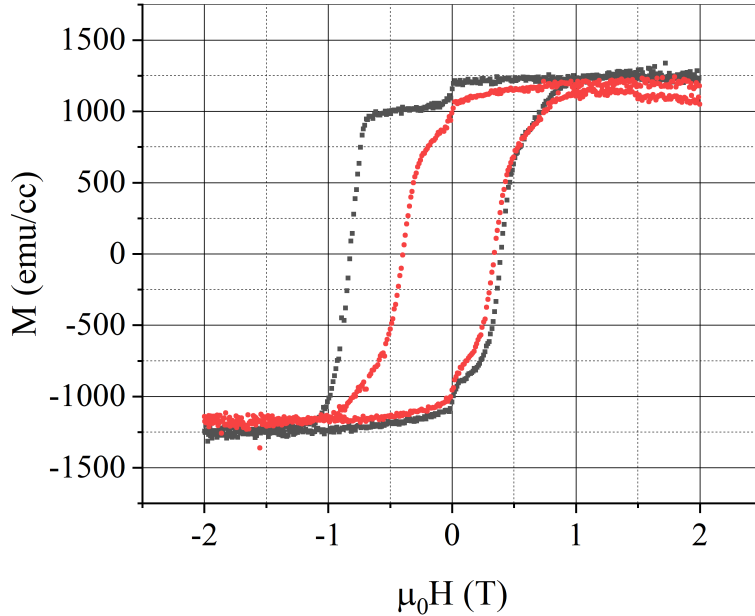


Figure 4.1: Consecutive hysteresis loops of a Ta(4nm)/Co(2.7nm)/C<sub>60</sub>(20nm)/Al(8nm) multilayer, field cooled from 120K to 3K. First sweep (black), second sweep (red).

## 4.2 Temperature Dependent VSM

To ascertain whether this pinning effect in field cooled samples is due to an exchange spring, or exchange biased system, temperature dependent hysteresis loops were measured. To ensure that any differences measured are due to temperature variation, all measurements were taken in the same measurement cycle so z-centring and the mounting position in the VSM weren't additional sources of variation. The freezing temperature of C<sub>60</sub> has been measured to be 90K [56, 57], although thermal fluctuations still occur within the system, so the timescale at which switching between orientations occurs is greater than that of taking a measurement (according to a Boltzmann distribution of temperatures). This meant the system had to be at a very stable temperature before taking a measurement since small changes in temperature would cause a large change in the negative coercivity of the first sweep. Thus, when the desired temperature was reached, the system was left for at least half an hour before taking a measurement to ensure thermal drift within the sample was mitigated. The hysteresis

## 4.2 Temperature Dependent VSM

---

curves at varying temperatures are given in Figure B.2 after being processed to remove the diamagnetic contribution from the sample holder, sample substrate and teflon tape.

For an exchange spring system, the temperature dependence of the coercivity is reliant on the hard layer's behaviour (in this case C<sub>60</sub>) [70–72]. The coercivity of any ferromagnet can be mapped to Kneller's law (see Equation B.3) [73]. If instead, this is a simple EB system, the temperature dependence of the EB is expected to have a linear or inversely proportional relationship to temperature [74, 75]. However, for partially frustrated spin systems such as this, exchange bias has been fitted to an exponential decay [22]. The temperature relationship with EB has been plotted and fitted to each of these functions (see Figure 4.2a), with a maximum exchange bias above 230mT. This value is much larger than has been reported in literature for hybrid organic/inorganic systems [22]. A similar curve for the first reversal coercivities against temperature can be found in Figure 4.2b. Clearly, linear and inversely proportional relationships do not hold for this system. However, both Kneller's law (exchange spring) and exponential decay (partially frustrated FM/AFM) agree very well with the measured data. Thus, from this data alone, the system could be a pure exchange spring system in which C<sub>60</sub> cages are rotated from a HP geometry to a H or P geometry at negative saturation, which has a lower anisotropy, causing the reduction in coercivity for the second reversal. Or, to a partially frustrated FM/AFM system. Coercivities were determined by using the ‘Level Crossing’ application in Origin. This introduces a small, undeterminable error in coercivity as it assumes a straight line between adjacent points in a hysteresis loop. The blocking temperature was calculated as 94K (see Fig B.3) which shows good agreement with the temperature at which rotational orientations of C<sub>60</sub> are frozen out. This could be an effective Néel temperature at which AFM ordering occurs, although this is phenomenologically different to the Néel temperature of a metallic AFM as this corresponds to a phase transition temperature as opposed to a spin ordering temperature in typical antiferromagnetic materials. And, the blocking temperature is usually below the Néel temperature [74], although accumulated error in determining coercivities, fitting and error intrinsic to the measurement could account for this as the absolute theoretical sensitivity of the Oxford Instruments VSM is 10<sup>-5</sup>emu and measured samples have saturation moments of the order 10<sup>-4</sup>emu.

$$\mu_0 H_c = \mu_0 H_c^0 [1 - (T/T_B)^\alpha] \quad (4.1)$$

### 4.3 Thickness Dependent VSM

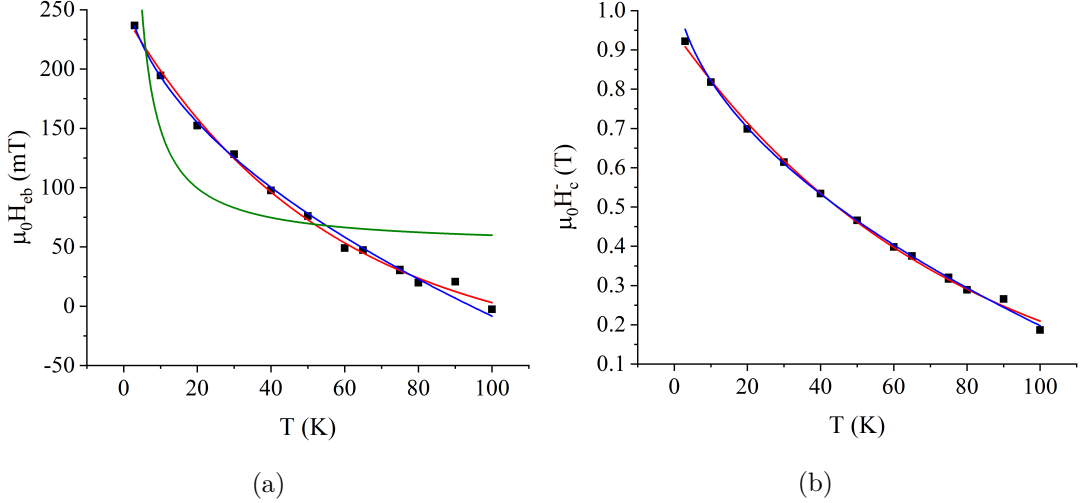


Figure 4.2: Temperature dependence of a) exchange bias and b) first reversal coercivity in a Co(2.7nm)/C<sub>60</sub>(20nm) bilayer with fitted curves: exponential decay (red), Kneller's law (blue) and  $1/T$  (green). Fitting parameters can be found in Tables B.2, B.3. Note: parameters for the green curve were omitted due to poor fitting.

### 4.3 Thickness Dependent VSM

Cobalt thickness dependence of this pinning effect was investigated to determine the optimum composition and calculate the energy product to assess this material's usefulness in a scaled magnet. C<sub>60</sub> thickness was not investigated as the optimum value of 20nm has already been determined by T. Moorsom [76]. To ensure maximum uniformity, all samples had the same seed and capping layer thicknesses, and all measurements were field cooled from 120K to 3K. This introduces additional variations in the z-centering and diamagnetic background contributions, although this was minimised by data processing. The result of this investigation for samples grown in the same vacuum cycle can be seen in Figure 4.3. The y-axis is plotted as both the effective exchange bias (4.3a), half the sum of the left and right coercivities, as this is the generally accepted way of measuring EB [22]. And as the first reversal coercivity (4.3b). Non-conformity of samples with Co thickness less than 3nm occurs in all FM/AFM systems (AFM oxides, metals and organics) and has been suggested to be due discontinuities in the FM layer [22, 77]. Epitaxial growth methods may be able to overcome this but this is expensive and time intensive.

### 4.3 Thickness Dependent VSM

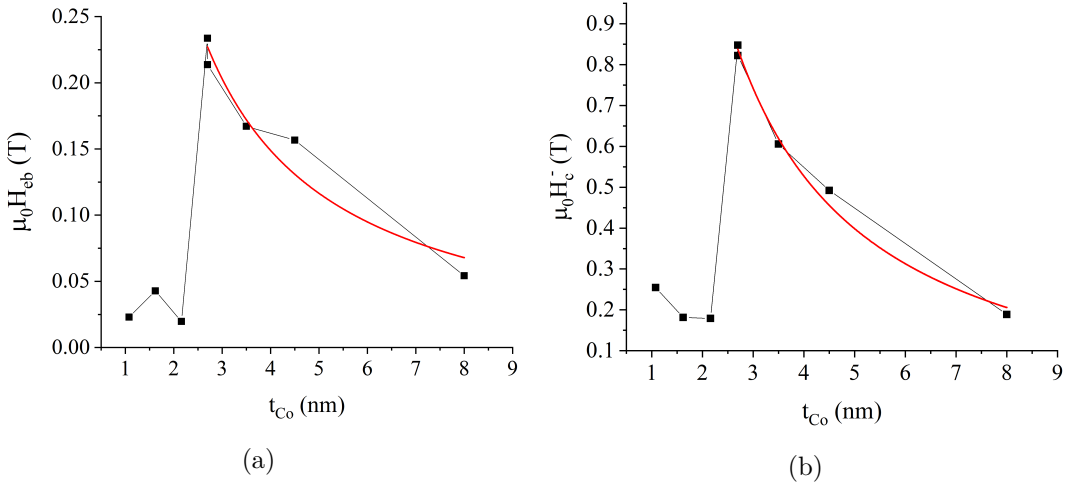


Figure 4.3: Cobalt thickness dependence of a) the effective exchange bias and b) the first reversal coercivity in field cooled  $Co(t \text{ nm})/C_{60}(20\text{nm})$  bilayers. Fitted equations are  $\mu_0 H_{eb} = \frac{0.649}{t} - 0.013$  (a) and  $\mu_0 H_c^- = \frac{2.575}{t} - 0.116$  (b).

Of the samples measured, the largest energy product was  $251 kJm^{-3}$  at 3K in one of the two  $Co(2.7\text{nm})/C_{60}(20\text{nm})$  samples. Interestingly, the second largest energy product was a sample of the same composition at  $235 kJm^{-3}$  (see Figure 4.4). To obtain a more accurate optimal composition, further investigation of samples near this composition will be required. This value is large, the first NdFeB magnets had values between  $110 - 290 kJm^{-3}$  in their bulk, sintered form [2, 3]. Thus, if this phenomena can be produced at higher temperatures, and in a bulk magnet using cobalt nanoparticles suspended in an organic matrix as a possible delivery method, the number of pinning sites per Co would be increased, as would the effective exchange coupling. This would further increase the coercivities of these systems to levels that could yield energy products larger than early NdFeB magnets, if not current, market leading iterations. In the figure below (4.4), the shape of the hysteresis loops are significantly different, despite these samples being of the same composition and produced in the same growth cycle. The red curve shows a clear vertical domain switching at zero field as evidence of exchange spring behaviour, whereas the green curve shows a gradual decline suggesting magnetisation dynamics closer to coherent rotation or slow domain wall propagation. This could be due to the existence of a pinning site nucleating magnetisation reversal in the red curve which is absent in the sample that produced the green curve. To

confirm this, XMCD or Kerr microscopy would have to be employed, although Kerr microscopy would have limited resolution due to the non-linear optical effects of C<sub>60</sub>. This highlights that small differences in Co surface texture and crystal structure have large influences on this effect and that another delivery method will be required for commercial magnets to ensure uniformity across samples.

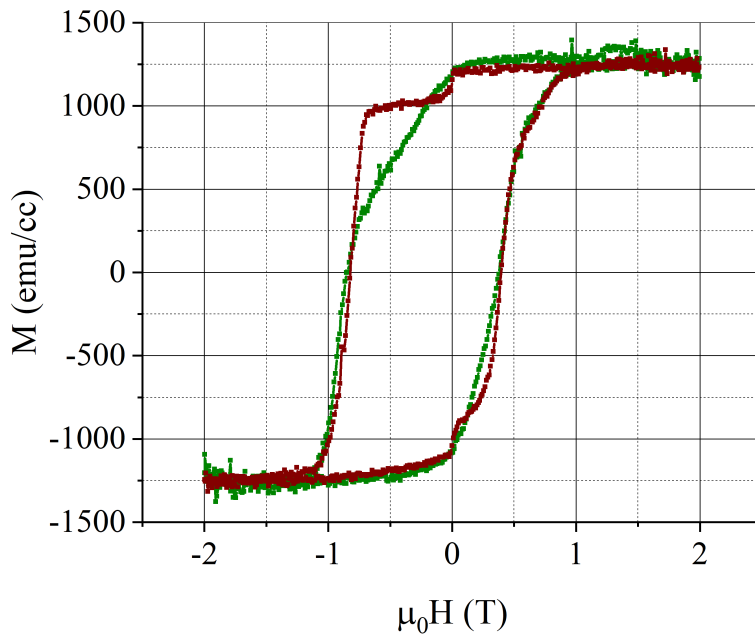


Figure 4.4: Hysteresis loops of two FC Co(2.7nm)/C<sub>60</sub>(20nm) samples, highlighting the large difference in hysteresis character between samples.

#### 4.4 C<sub>70</sub> Fullerene

One of the most interesting avenues of investigation to understand the phenomena in Co/C<sub>60</sub> bilayers was to substitute the C<sub>60</sub> for another material with similar electronic properties, but fewer rotational degrees of freedom. C<sub>70</sub> is, structurally, very similar to C<sub>60</sub> with the addition of a ring of hexagons along its equator (see Figure B.5), so was chosen for this purpose. The addition of hexagons along the equator produces an ellipsoidal shape, reducing the rotational degrees of freedom to two: spinning along its equator and spinning about the plane of deposition - compared to the three rotational degrees of freedom of C<sub>60</sub>. In addition, about the equator of the minor ellipsoid axis,

it possible that it has an energy barrier less than 0.2eV between similar orientations. Although, the study of C<sub>70</sub> is much less common than C<sub>60</sub>, so this is uncertain. If this is the case, lesser pinning in field cooled samples is expected, and a lower blocking temperature. However, if this is not the case, the converse is expected to be true. Below, the relationship between temperature and both effective exchange bias (4.5b) and first reversal coercivity (4.5b) is plotted for Co(3nm)/C<sub>70</sub>(20nm) - a similar composition as Figure 4.2.

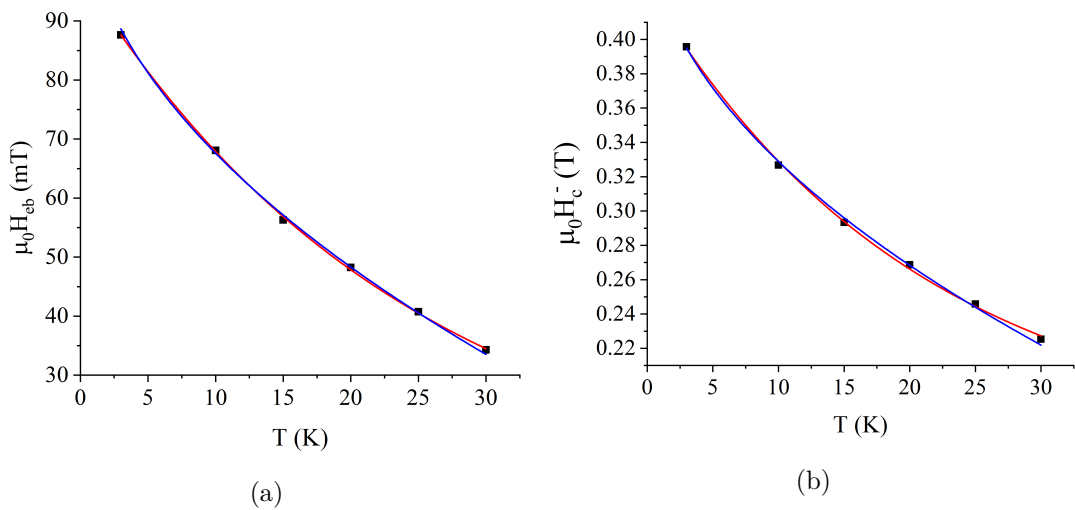


Figure 4.5: Temperature dependence of a) exchange bias and b) first reversal coercivity in a Co(3nm)/C<sub>70</sub>(20nm) bilayer with fitted curves: exponential decay (red), Kneller's law (blue). Fitting parameters can be found in Tables B.2 and B.3.

This C<sub>70</sub> sample shows a much smaller pinning effect than C<sub>60</sub> samples: coercivity of Co/C<sub>70</sub> at 3K was measured to be 0.4T, whereas a C<sub>60</sub> sample at the same temperature was measured to be 0.9T. The blocking temperature is also reduced at around 60K (see Fig B.2). This suggests that deposited C<sub>70</sub> has a very small energy barrier between orientations along the equator. This means it is likely for only two energetically favourable geometries to be present in adsorbed molecules (HH and H). Similarly, FM coupling, which produces an enhanced coercivity compared to a bare cobalt layer, is smaller than in C<sub>60</sub> samples. The value of the second sweep coercivity at 30K for Co(3nm)/C<sub>70</sub>(20nm) was 0.16T, and 0.36T for Co(2.7nm)/C<sub>60</sub>(20nm). The cobalt layer thickness is slightly different, however, a difference of 0.2T is more likely due to the different molecule used than the structure of the cobalt film. Although, the

## 4.5 Surface Roughness

---

fitted curve of Figure 4.3 would suggest 3nm cobalt thickness corresponds to a coercivity of around 0.2T. But, 2.7nm has not been identified as the optimal composition, so this thickness may correspond to a value higher than 0.36T.

### 4.5 Surface Roughness

Part way through this project, the Ta target in the sputtering system was replaced as the old target was very thin. This thinness meant that there was uncertainty in the growth as the sputter rate varies drastically between growths. And, if the target sputtered through, the samples in that growth cycle could not be used as their structure would be unknown. This change of target produced samples of Co/C<sub>60</sub> that showed much less pinning than previously grown samples (0.3T coercivity, see Fig B.7). Initial conclusions were that this target produced an interface with higher roughness than the old target. However, this was counter-intuitive. The new Ta target had a higher purity (99.999% rather than 99.995%) so it would be expected that this produced higher quality films. XRR data (see Fig 4.6) was taken for calibration samples of both targets and curves were simulated using a Bruker software package (Bede). This simulation software minimises the differences between data and simulated curves by changing the parameters density, roughness and thickness. The inclusion of multiple layers allows density variation as a function of depth. The density is related to the quality of the crystal structure, with 100% density attributed to a single crystal, whereas lower values are due to lengthening of the average lattice constant from grain boundaries and imperfections. This showed that the new Ta target had a total stack roughness of 26Å compared to 17Å for the old target (see Table B.4), this increase in roughness produces comparable roughness in the Co layer which reduces the number of pinning sites for C<sub>60</sub> adsorption. This presents a viable explanation of the reduced pinning observed when using the new Ta target. Although, further investigation using atomic force microscopy and XMCD would probe surface texture and differences in magnetisation dynamics more accurately - this would not be possible with Kerr microscopy due to the thick Al and C<sub>60</sub> layers. This further cements the importance of a smooth interface for these effects to occur. The lower roughness of the less pure target is attributed to a smaller grain size and impurities increasing the surface mobility of atoms, producing a smoother Ta seed.

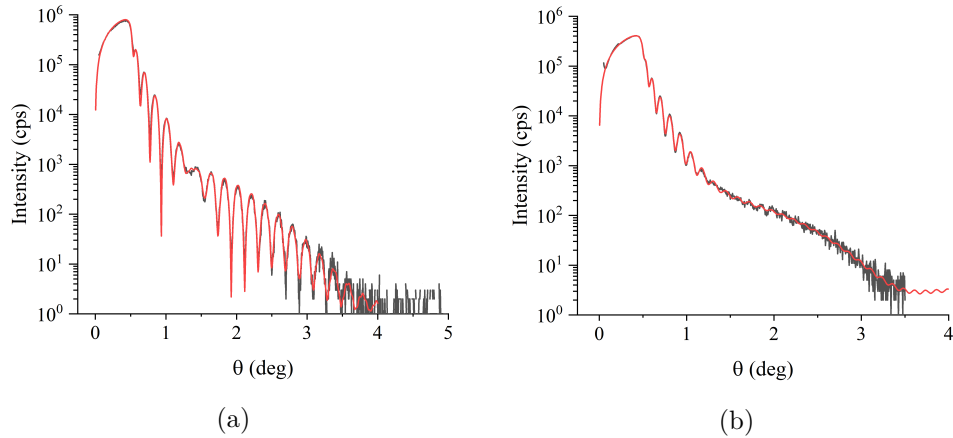


Figure 4.6: XRR data (black) of a 20nm calibration of the old Ta target (a) and a 30nm target of the new Ta target (b) with simulated curves in red. Values of fitted parameters can be found here [B.4](#).

## 4.6 Micromagnetic Modelling

To compliment experimental work, modelling of these systems was undertaken. Mumax3 was used as this is a versatile, open source, finite difference micromagnetic simulation package that allows many different phenomena to be modelled, including exchange bias, 3D grains (to replicate surface roughness) and variable interlayer exchange coupling. Mumax3 3.10 $\beta$  was used as this has additional functionality over the most recent stable release (3.9 at the time of writing). Although, this presented difficulties, for large simulations (usually including 3D grains due to more intensive calculation) this led to a metastable solution in which magnetisation would remain near zero (see Figure C.2). This meant that simulation boxes had to remain small, as semi-infinite calculations (ie a similar size to samples produced in the lab) proved too large, incurring this error. Antiferromagnets are not directly modelled using this software, however, a ferromagnet can be used with equal  $M_s$  to the FM being modelled and its demagnetising field switched off so that non-atomistic calculations are equivalent to those for an AFM since only adjacent grains (ie interfacial grains) experience any effect from this pseudo-AFM through the exchange coupling constant (labelled as  $A_{ex}$  in this software see Eq 4.3 and 4.4) and intergrain exchange scaling (exchange coupling between specific regions can be multiplied by some factor) which is defined in the input script. This is acceptable

## 4.6 Micromagnetic Modelling

---

for a micromagnetic model in which many individual spins are substituted with cells of finite dimensions ( $\sim \mu\text{m}$ ) and is given bulk values for different parameters. This allows spin dynamics to be modelled using a classical equation (Eq 4.2 is the form of the LLG equation used by Mumax3), the numerical solutions of which produce the magnetisation dynamics of the system. In magnetic materials, spins do not point in a fixed direction, but precess about a fixed axis. In the case of a ferromagnet in a saturating magnetic field, the spins precess about the axis of the applied field. This precessional motion has a damping factor to ensure the system relaxes to an equilibrium state for a given set of extrinsic parameters. In real systems, the damping comes from the Gilbert damping parameter which has been derived from the expansion of the Dirac equation, and has been attributed to the dynamics of SOC [78] - this is an intrinsic property of a given material. For micromagnetic simulations,  $\alpha$  is the damping parameter of the system and influences how quickly the system will reach an equilibrium state. The effect of anisotropy and other effects are implemented by an effective field embedded in the  $H_{eff}$  (see Eq 4.2). For the purpose of this report,  $\alpha$  is kept as the default value as the dynamics of the magnetisation are not investigated and hysteretic properties are modelled without the evolution of time. All simulations are modelled in a zero temperature environment due to the lack of thermal training observed experimentally in Co/C<sub>60</sub> system (see Section 2.4).

$$\frac{dM_s}{dt} = \frac{\gamma\mu_0}{1+\alpha^2} M_s \times H_{eff} - \frac{\alpha\gamma\mu_0}{M_s(1+\alpha^2)} M_s \times (M_s \times H_{eff}) \quad (4.2)$$

$$A_{ex} \approx \frac{k_B T}{2a_0} \quad (4.3)$$

$$E_{ex} = A_{ex}(\nabla\mathbf{m})^2 \quad (4.4)$$

The interlayer exchange between different materials is calculated by a harmonic mean [79], and, the use of the interlayer exchange scaling allows pinhole contact and other interface dependent effects to be accurately modelled by decreasing the average interlayer coupling to values obtained from experimental results: simple calculations of this for an EB system assumed a perfect interface and were estimated to be of the order of  $100mJ m^{-3}$  which is three orders of magnitude higher than in FeMn which has been

## 4.6 Micromagnetic Modelling

---

measured to be  $0.1mJ\ m^{-3}$  experimentally [80].

Initial simulations were of a thin film exchange spring of dimensions  $(320 \times 320 \times 6)\text{nm}$ , with one polycrystalline bcc Co layer (see Section 3.1) with parameters  $M_s = 1.4 \times 10^6\text{Am}^{-1}$ , exchange stiffness  $A_{ex} = 30pJm^{-1}$  and uniaxial anisotropy constant  $K_1 = 2 \times 10^4\text{Jm}^{-3}$ . Uniaxial anisotropy axis was the x-axis (100) with a random misalignment introduced to each grain with 10% standard deviation. Above this, a harder ferromagnetic material was modelled. This was given the same saturation magnetisation as Co (to ensure even splitting of energy across the interface when an AFM is introduced [81]), exchange stiffness of  $4pJm^{-1}$  and uniaxial anisotropy constant of  $2 \times 10^6\text{Jm}^{-3}$ , and similar anisotropy axis initiation. This is an unconventional setup given the stiffness of the hard material is less than the soft material. This implies a smaller  $T_c$  of the hard material (approximated by Eq 4.3). This was introduced as a precursor to the introduction of an AFM layer since it is expected that the Néel temperature is smaller than the Curie temperature for exchange bias to be observed. Both the total magnetisation of the stack, and magnetisation of individual layers was given as an output. The total magnetisation of this simulation can be seen below in Figure 4.7. This hysteresis shows good agreement with experimental results for a system of this type (see Figure A.10) with a well defined two phase switching mechanism.

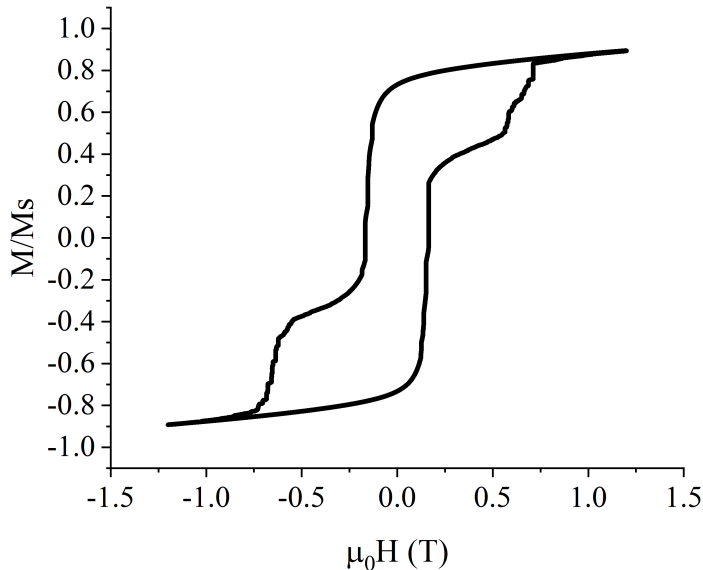


Figure 4.7: Simulated hysteresis curve of an exchange spring.

## 4.6 Micromagnetic Modelling

---

Follow up simulations were to identify the effect of rotatable antiferromagnetic grains on the behaviour of the ferromagnetic layer [82, 83] (see Figure 4.8). This was implemented by using the same script as for above with the inclusion of no demagnetising contributions from the magnetically hard layer. Thus, coupling between the two layers isn't influenced by the ferromagnetic behaviour of the hard layer. This is equivalent to an AFM with no net magnetisation. This has produced a hysteresis loop that looks like bare cobalt at first glance, however, an increase in coercivity is observed (approximately one order of magnitude higher) due to the pinning of cobalt grains at the interface (see Figure C.3). This is precisely equivalent to an exchange spring system if only the magnetisation of the soft layer is considered. And, as expected, no exchange bias was observed. This is because interfacial AFM grains coupled to the FM have an anisotropy constant small enough to be able to be rotated between positive and negative spin orientations in the direction of applied field by the combined contributions of the demagnetising field of the FM and the externally applied field, so FM grains are not pinned by these rotating AFM grains.

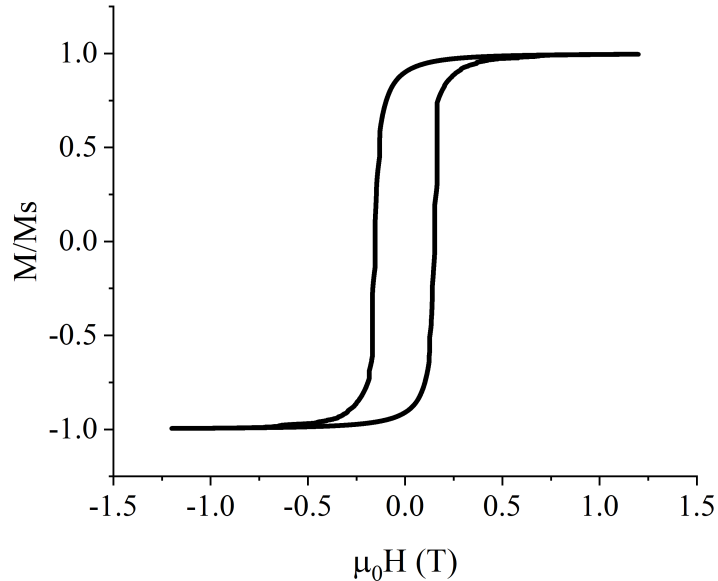


Figure 4.8: Simulated hysteresis of the ferromagnetic layer of a two layer system consisting of a FM and an AFM with rotatable grains.

Exchange bias was also simulated by attributing a value of the anisotropy  $K1 = 2.7 \times 10^7 Jm^{-3}$  (this value was taken from [81]). This is sufficiently large that AFM

## 4.6 Micromagnetic Modelling

---

grains won't rotate with the combined contributions of the demagnetising field and external applied field [81], pinning FM grains at the interface, producing exchange bias (see Figure 4.9). The field cooling procedure was implemented by setting the magnetisation as uniform in the applied field direction, then relaxing the system in a 2T field. Note, this curve has a much smaller coercivity than Fig 4.8 due to a lack of rotatable AFM grains.

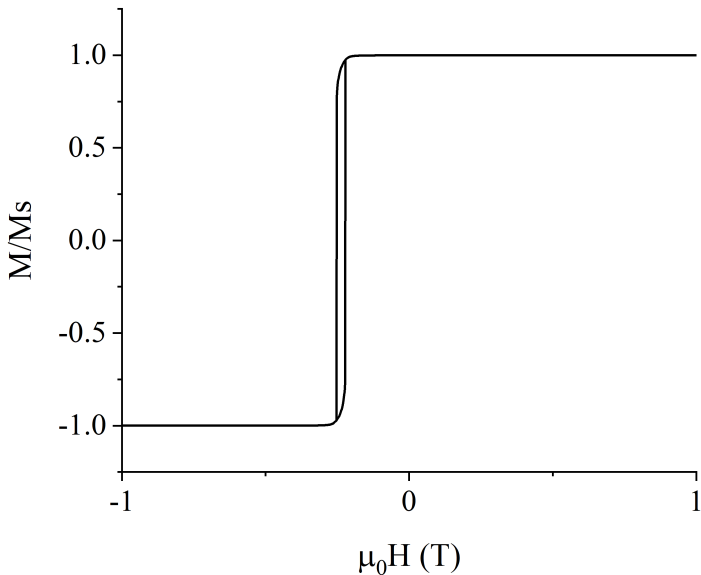


Figure 4.9: Simulated hysteresis of an exchange biased system attributed to pinned AFM grains.

After these phenomena were confirmed to be implemented correctly in Mumax3, Co/C<sub>60</sub> bilayers were modelled. The FM was given properties as discussed at the beginning of this section. All AFM grains were given an exchange stiffness of  $4pJm^{-1}$  and the majority of AFM grains were given an anisotropy of  $2 \times 10^6 Am^{-1}$  to simulate exchange bias. However, a third of these grains were given an anisotropy of  $5 \times 10^5 Am^{-1}$  to simulate rotatable grains and produce the increase in coercivity which is observed experimentally. To replicate the switching mechanism observed in Co/C<sub>60</sub> systems, after the first reversal of magnetisation, pinned grains had their anisotropy reduced to the same value as rotatable grains. Thus, for subsequent reversals, no exchange bias was observed. This can be seen below in Figure 4.10. To obtain a curve that agreed with experimental results, an iterative process of refining the value of the anisotropy

## 4.6 Micromagnetic Modelling

---

constant for the  $C_{60}$  layer and interlayer exchange coupling between Co and  $C_{60}$  was used. The figure above used a value of  $K1 = 5 \times 10^5 Am^{-1}$ . A comparison of the first and final simulated Co/ $C_{60}$  shows the importance of this process (see Figure C.1). Further simulations would improve hysteresis texture and the values of coercivity to replicate that of real samples by fine tuning parameters including grain size, anisotropy constants and directions, and intergrain exchange coupling. Plus, the implementation of a grain structure in the FM would simulate the polycrystalline nature of real systems, giving the hysteresis more texture and show more complex switching dynamics. However, due to the limitations discussed earlier, this was not possible. And, inclusions of the temperature dependence of this effect would not be able to reproduce what is observed experimentally due to the molecular nature of the system, unless custom code is produced which includes values for energy barriers and fine energy structure of the molecular systems - this would be computationally intensive and it could be argued that DFT models would be easier to implement as quantum levels are already implemented in specialised software packages.

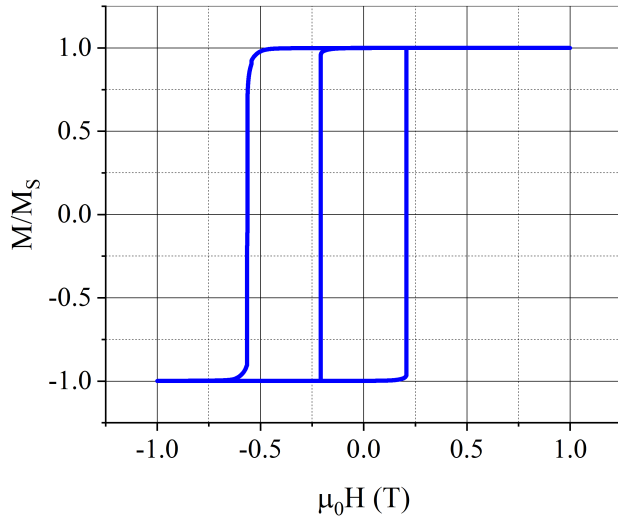


Figure 4.10: Two sweeps of a simulated Co/ $C_{60}$  system exhibiting both exchange bias and exchange spring phenomena.

---

# CHAPTER 5

---

Conclusion

---

This report has showcased that the source of enhanced coercivity in FC Co/C<sub>60</sub> bilayers is due to exchange bias with a unique training mechanism induced by the irreversible switching of C<sub>60</sub> cages through the magnetic torque applied by an external field. And, that samples show exchange spring behaviour, after exchange bias has been destroyed, through an increase in coercivity as compared to bare cobalt which has been confirmed through micromagnetic simulation and previous DFT models. This is a more complex mechanism than has been proposed by literature thus far and presents a new direction of study for organic/metal systems to better predict the behaviour of these materials. This guides research to study molecules which are highly electronegative to induce orbital hybridisation, have multiple adsorption sites with energy barriers of around 10meV per atom in the molecule which is expected to produce this effect at room temperature.

As this research has presented a full set of mechanisms for the enhanced coercivity and exchange bias in Co/C<sub>60</sub> bilayers, future research should focus on identifying molecules with these properties to produce increased coercivities at higher temperatures in thin films through the collaboration of condensed matter physicists and chemical scientists, which is increasingly prevalent through the study of molecular magnetism. And, to investigate possible delivery methods which can deliver up to 0.9T coercivities in bulk magnets. The molecules could be in the form of aromatic compounds with similar symmetries to C<sub>60</sub>, with the addition of a lipid tail which would provide the large energy barriers between orientations. And, delivery methods of metallic nanoparticles suspended in resin or polymer compounds which are set in a magnetic field in a similar process to sintering in NdFeB magnets, but at much lower temperatures increasing the efficiency of the manufacturing process. This will further increases anisotropy by producing many pinning sites with approximately uniform anisotropy direction. Or, MOFs could be employed to introduce both hybridisation and a stable structure for magnets that don't degrade, as long as the ferromagnetic clusters are large enough to not exceed the superparamagnetic limit. This would reduce the reliance on a smooth interface for bilayer structures and mitigate the use of additional materials like Ta and Al which do not contribute to the effect but provide a smooth surface and increase the longevity of samples by preventing oxidation. It would be prudent to investigate the causes of failed interfaces as discussed in Section 4.1 to further understand the dynamics of the molecular interface. Although, this would likely require the use of a TEM

---

as x-ray experiments are dependent on the transparency of materials used, and the nonlinear optical effects of C<sub>60</sub> would make this difficult to discern any real structural characteristics from artefacts of the nonlinear system.

The investigation of PMA configurations of Co/C<sub>60</sub> bilayers would be interesting as the perpendicular nature may lead to a compensated AFM interface which would not produce EB. This is important for verifying this material's usefulness, not only in bulk permanent magnets, but in non-volatile persistent magnetic memory for computing applications.

# Appendices

---

# APPENDIX A

---

Properties of Magnetic Materials

Parameter		H	H	B
	Units	$\text{Am}^{-1}$	Oe	Tesla
H	$\text{Am}^{-1}$	1	$4\pi \times 10^{-3}$	$\mu_0$
H	Oe	$10^3/4\pi$	1	$10^{-4}$
B	Tesla	$1/\mu_0$	$10^4$	1

Table A.1: Magnetic field conversion table. Conversions are from *row* value to *column* by multiplying by the value in the table.

Parameter		M	M
	Units	$\text{emu/cc}$	$\text{emu/g}$
M	$\text{emu/cc}$	1	$1/\rho$
M	$\text{emu/g}$	$\rho$	1

Table A.2: Magnetisation conversion table. Conversions are from *row* value to *column* by multiplying by the value in the table.

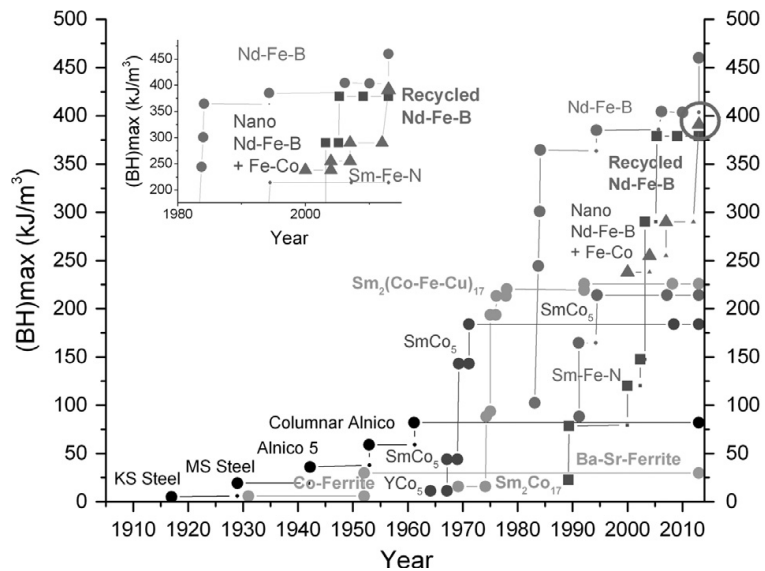


Figure A.1: Historical development of different types of permanent magnets, plotted against their maximum energy products  $(\text{BH})_{\text{max}}$ . Printed from [84].

---

	$T_C$ (K)	$m$ ( $\mu_B$ /atom)	$M_s$ ( $kAm^{-1}$ )	$\mathcal{N}_{\uparrow\downarrow}(\epsilon_F)$ (eV)	$I$ ( $eV^{-1}$ )
Fe	1044	2.17	1710	1.54	0.93
Co	1360	1.71	1440	1.72	0.99
Ni	628	0.58	488	2.02	1.01

Table A.3: Intrinsic properties of the ferromagnetic 3d elements at room temperature. Adapted from [85].

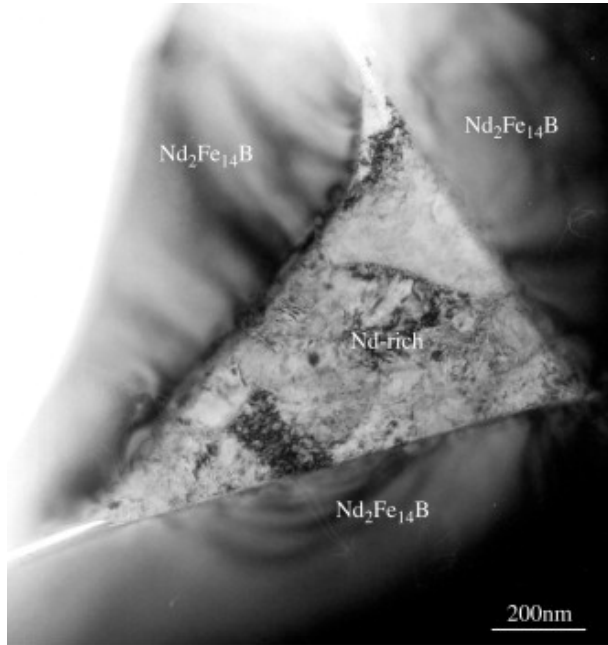


Figure A.2: Bright-field TEM micrograph of a NdFeB magnet, showing  $Nd_2Fe_{14}B$  matrix grains and Nd-rich grain boundary phase. Printed from [86].

$$\mathcal{H} = -\mathcal{J} s_1 \cdot s_2$$

Figure A.3: Exchange Hamiltonian,  $\mathcal{H}$ , for direct exchange (ie the 3d ferromagnets Fe, Co, Ni) between two adjacent spins  $s_1$  and  $s_2$ .  $\mathcal{J}$  is the exchange constant. In ferromagnets,  $\mathcal{J}$  is positive which produces an energy minimum when spins are parallel and a maximum when spins are antiparallel.

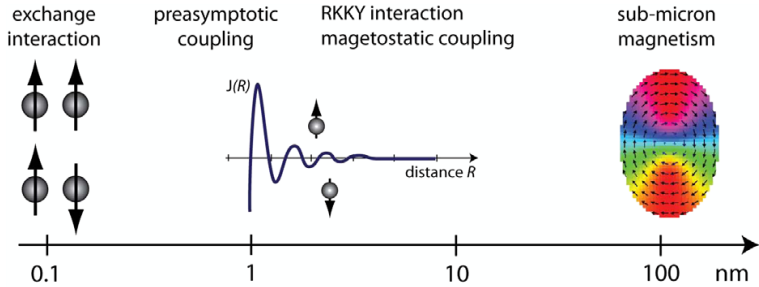


Figure A.4: Relevant length scales in magnetism. Printed from [87].

$$U = \Lambda \mathbf{L} \cdot \mathbf{S}$$

Figure A.5: Energy due to the spin-orbit interaction where  $\Lambda$  is the SOI coupling constant and is dependent on the element considered,  $\mathbf{L}$  is the orbital angular momentum of electrons in an atom and  $\mathbf{S}$  is the net spin of the electronic structure of an atom according to Hund's rules.

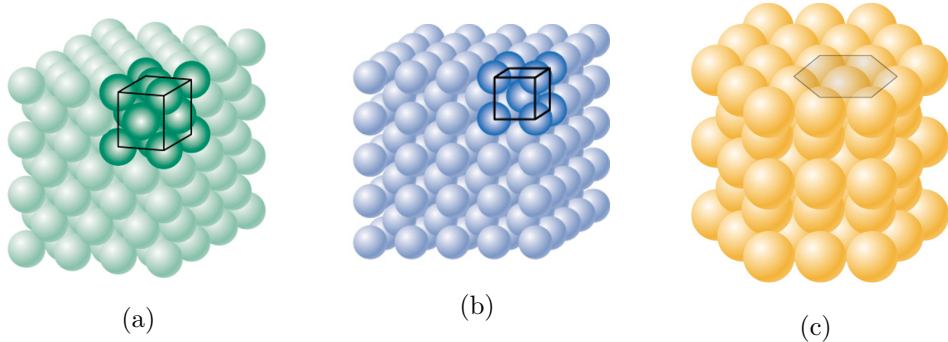


Figure A.6: Example crystal lattice structures: a) FCC b) BCC c) HCP.

$$E = K_1(\alpha^2\beta^2 + \beta^2\gamma^2 + \gamma^2\alpha^2) + K_2(\alpha^2\beta^2\gamma^2)$$

Figure A.7: Cubic anisotropy energy density to second order.  $K_1$  and  $K_2$  are the first and second order anisotropy constants, resp. and are measured in  $Jm^{-3}$ .  $\alpha$ ,  $\beta$  and  $\gamma$  are the direction cosines of the magnetisation. More rigorously, magnetisation is given as  $\mathbf{M} = M_x\hat{i} + M_y\hat{j} + M_z\hat{k}$  and  $\alpha$  is given as  $\frac{M_x \cdot \hat{i}}{|\mathbf{M}|}$ .  $\beta$  and  $\gamma$  are expressions of the same form with differing unit vectors.

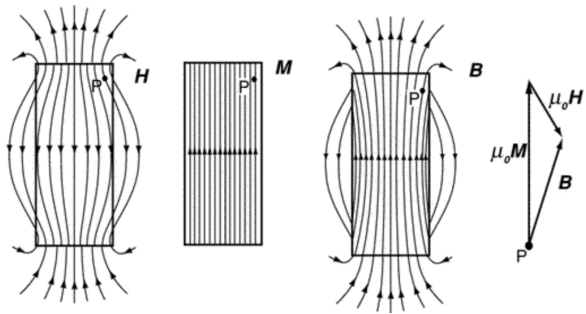


Figure A.8: Graphical representation of the relationship between  $B$ ,  $M$  and  $H$ . Printed from [80].

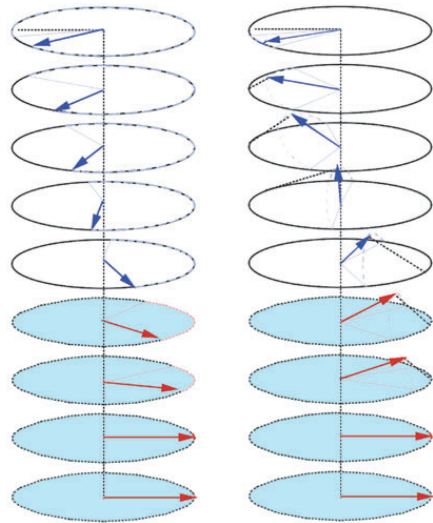


Figure A.9: Schematic representation of the spin structure of the hard and soft layer during reversal through (a) the Bloch-like mode and (b) the Néel-like mode. In the Néel-like mode, the spins rotate out of the plane of the film. Printed from [44].

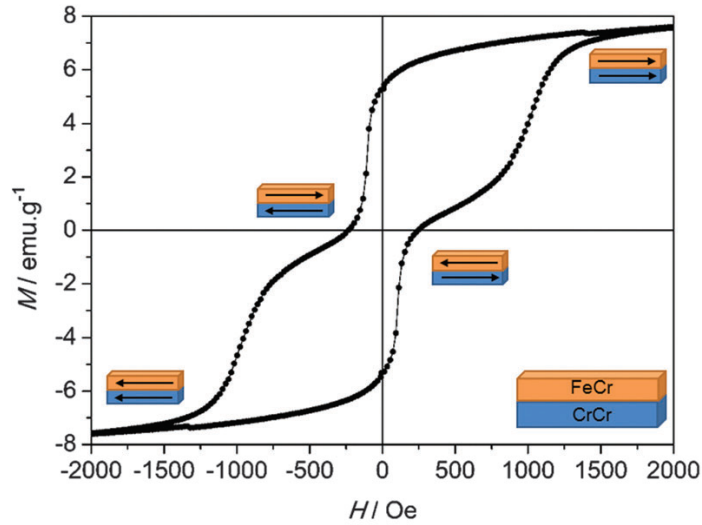


Figure A.10: Hysteresis of an exchange coupled bilayer which shows the switching of the soft and hard layers as distinct phases. Printed from [88].

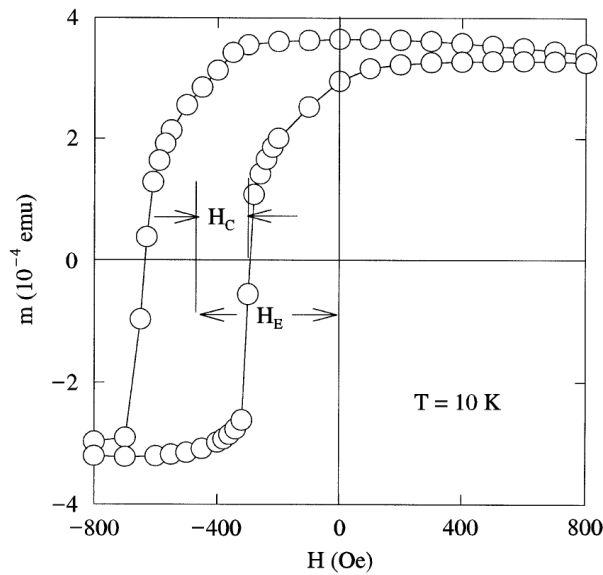


Figure A.11: Hysteresis loop of a field cooled  $\text{FeF}_2/\text{Fe}$  bilayer at 10K, indicating the exchange bias and coercivity. Printed from [77].

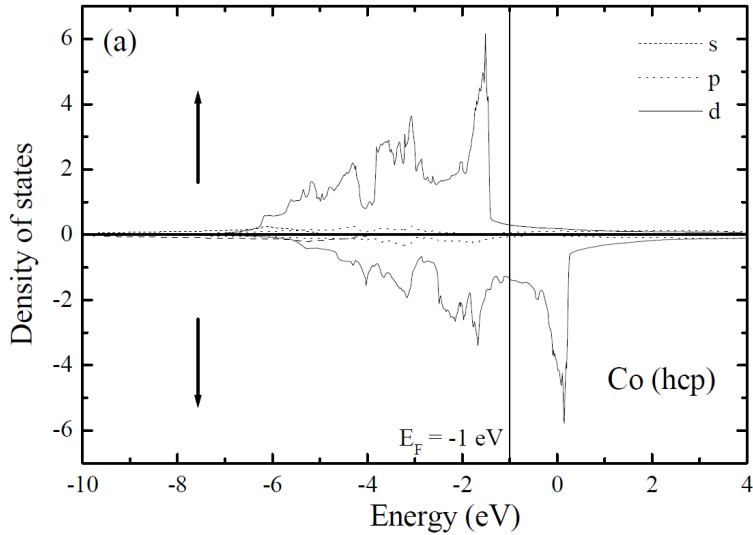


Figure A.12: Cobalt density of states, resolved into spin majority (top) and minority (bottom) bands. Printed from [89].

$$PV = Nk_B T$$

Figure A.13: The ideal gas equation.  $P$  is the pressure of the gas in  $Pa$ .  $V$  is the volume of the gas in  $m^3$ .  $N$  is the number of gas molecules.  $T$  is temperature in Kelvin. And,  $k_B$  is Boltzmann's constant (approximately  $1.38 \times 10^{-23} JK^{-1}$ ).

---

# APPENDIX B

---

Co/C<sub>60</sub> Bilayers

---

Adsorption site	$\Delta E$ (eV)	$E_{\text{ads}}$ (eV)	$\Delta M$ ( $\mu_B$ )	$M(\text{Co})$ ( $\mu_B$ )	$M(\text{C}_{60})$ ( $\mu_B$ )
H	+0.96	-5.50	-1.83	108.7	-0.20
P	+0.70	-5.76	-1.75	108.8	-0.14
HP	0.00	-6.46	-1.95	108.6	-0.12
HH	+0.21	-6.25	-2.56	107.81	-0.17

Table B.1: DFT calculation of a Co/C<sub>60</sub> bilayer between different adsorption orientations of C<sub>60</sub> on the Co lattice.  $\Delta E$  represents the energy barrier between orientations with respect to the HP geometry for one C<sub>60</sub> molecule.  $\Delta M$  is the change in Co magnetisation compared to a bare Co layer. M(Co) and M(C<sub>60</sub>) are the total magnetic moments for Co and C<sub>60</sub> in the model. This data was produced by Dr. Gilberto Teobaldi at the Scientific Computing Department, STFC RAL.

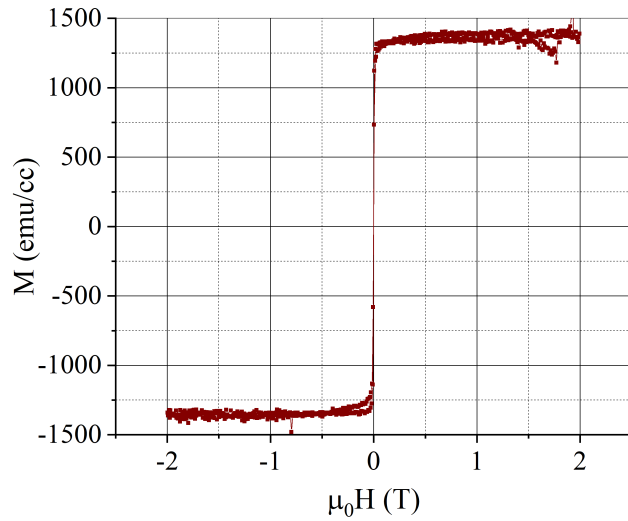


Figure B.1: Hysteresis loop of Ta(4nm)/Co(3nm)/C<sub>60</sub>(20nm)/Al(8nm), field cooled to 3K. This sample exhibited no pinning and a coercivity of the order of  $Oe$  and a magnetisation very close to literary value of 1440emu/cc ( $\approx 1380 \text{emu/cc}$ ).

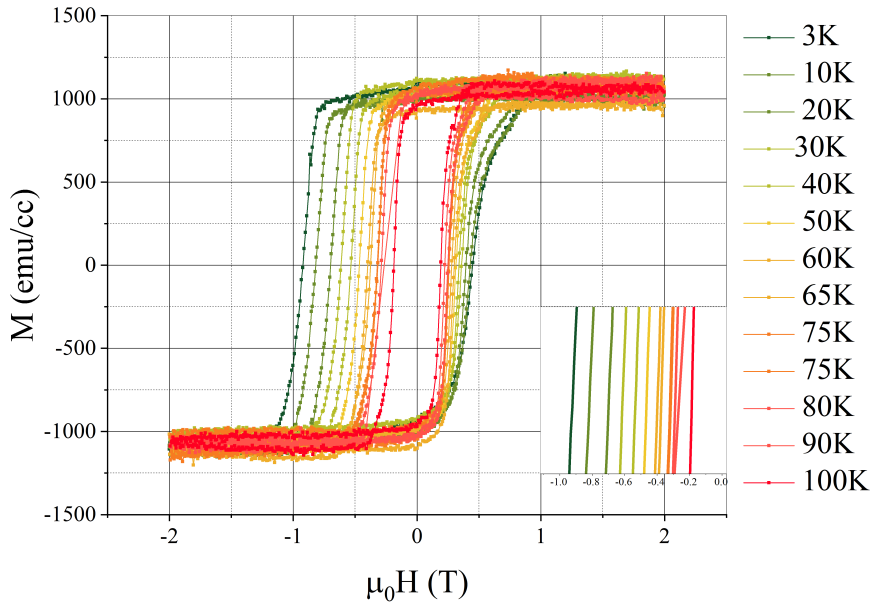


Figure B.2: Hysteresis loops of a Co(2.7nm)/C<sub>60</sub>(20nm) bilayer at various field cooled temperatures. Inset shows the same data, centred about the negative coercivities. Straight lines between points are included as a guide for the eye.

$$\mu_0 H_c = \mu_0 H_c^0 [1 - (T/T_B)^\alpha]$$

Figure B.3: Fitting function for Kneller's law (blue curves of Fig 4.2) and 4.5.  $\alpha$  was fixed to 1/2 as in [71, 72]. Fitted parameters can be found below.  $\mu_0 H^0$  is the zero temperature extrapolation of  $\mu_0 H$  and  $T_B$  is the blocking temperature.

---

Sample	Figure	$\mu_0 H^0$ (T)	$T_B$ (K)
Co(2.7nm)/C <sub>60</sub> (20nm)	4.2a	0.28725	94.473
Co(2.7nm)/C <sub>60</sub> (20nm)	4.2b	1.1107	148.06
Co(3nm)/C <sub>70</sub> (20nm)	4.5a	0.11415	60.137
Co(3nm)/C <sub>70</sub> (20nm)	4.5b	0.47506	105.66

Table B.2: Kneller's law fitting parameters, plotted as the blue curves in Figures 4.2 and 4.5.

$$\mu_0 H = \mu_0 H_{eb}^0 e^{\frac{-T}{\tau}} + C$$

Figure B.4: Exponential decay fitting function (red curves of Fig 4.2 and 4.5). A small constant  $C$  was included, but restricted to small values, to account for a small systematic error in the calculation of  $\mu_0 H$  discussed in Section 4.2. Fitted parameters can be found below.  $\mu_0 H^0$  is the zero temperature extrapolation of  $\mu_0 H$ , and  $\tau$  is some temperature scaling.

Sample	Figure	$\mu_0 H^0$ (T)	$\tau$ (K)	C (T)
Co(2.7nm)/C <sub>60</sub> (20nm)	4.2a	0.29154	54.564	-0.04345
Co(2.7nm)/C <sub>60</sub> (20nm)	4.2b	1.00973	76.258	-0.06257
Co(3nm)/C <sub>70</sub> (20nm)	4.5a	0.0903	24.7406	0.00763
Co(3nm)/C <sub>70</sub> (20nm)	4.5b	0.2666	0.1639	20.8751

Table B.3: Exponential decay fitting parameters, plotted as the red curves in Figures 4.2 and 4.5.

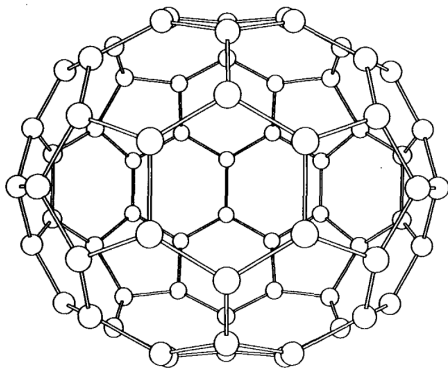


Figure B.5: Structural representation of  $C_{70}$ . Printed from [90].

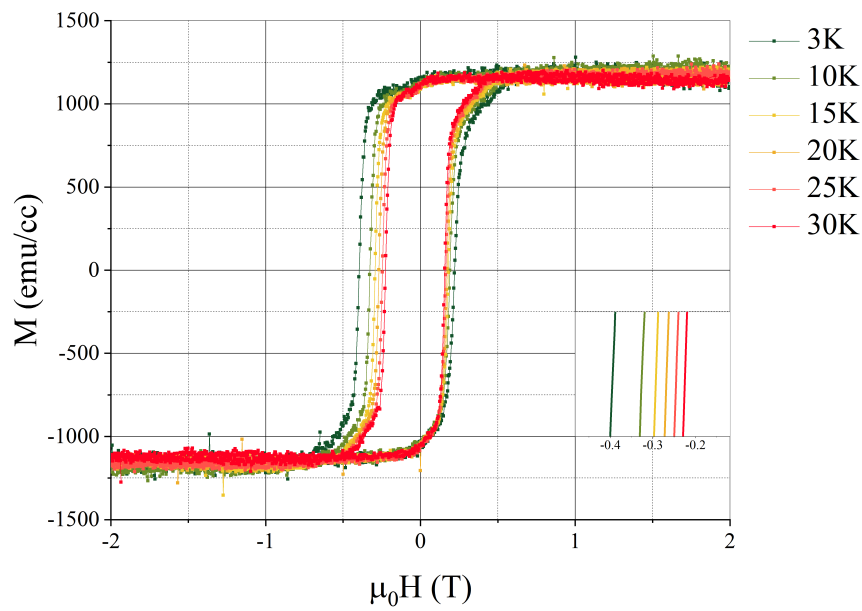


Figure B.6: Hysteresis loops of a Co(3nm)/C<sub>70</sub>(20nm) bilayer at various field cooled temperatures. Inset shows the same data, centred about the negative coercivities. Straight lines between points are included as a guide for the eye.

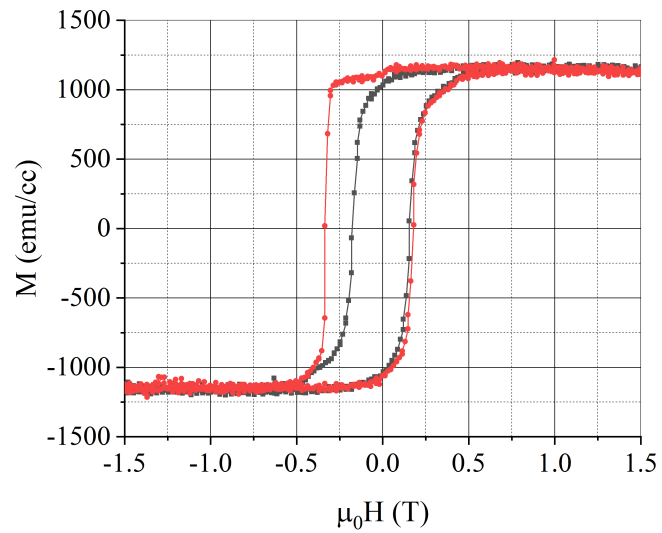


Figure B.7: Two consecutive hystersis curves of Ta(4nm)/Co(3nm)/C<sub>60</sub>(20nm) with the new Ta target. First sweep (red), second sweep (black). Coercivity of the first reversal measured as 330mT.

---

Sample: Old Tantalum			
Material	Thickness (Å)	Roughness (Å)	Density (%)
Si	$\infty$	0.00	100.00
SiO <sub>2</sub>	706.70	4.39	88.21
Ta	210.88	5.21	95.98
Ta	6.28	3.08	87.93
Ta <sub>2</sub> O <sub>5</sub>	16.05	4.42	92.36
Total	233.21	17.1	
Sample: New Tantalum			
Material	Thickness (Å)	Roughness (Å)	Density (%)
Si	$\infty$	0.00	100.00
SiO <sub>2</sub>	37.00	12.68	85.01
Ta	288.79	0.04	92.02
Ta	19.24	11.11	82.99
Ta <sub>2</sub> O <sub>5</sub>	0.14	2.35	99.55
Total	308.17	26.18	

Table B.4: Fitting data for the simulated XRR curves found here [4.6](#).

---

# APPENDIX C

---

Mumax3

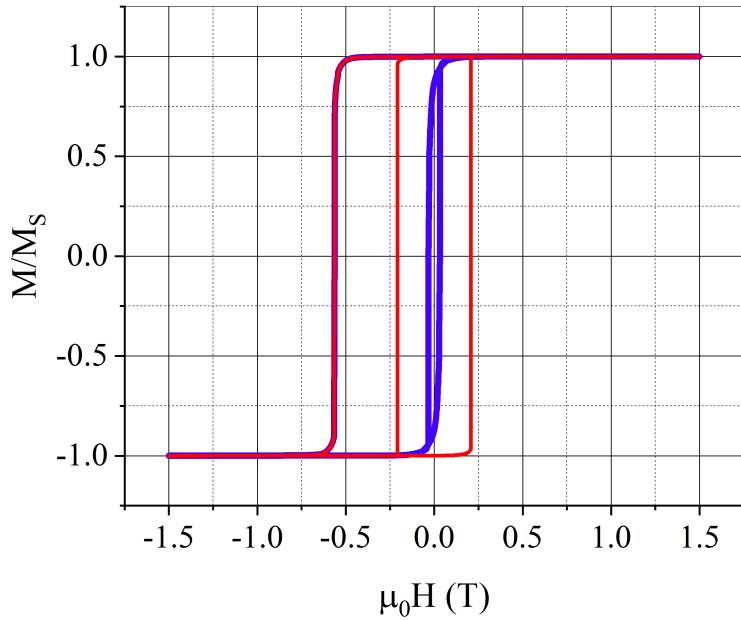


Figure C.1: Simulated hysteresis loops of a Co/C<sub>60</sub> bilayer with the inclusion of C<sub>60</sub> switching at negative saturation. The red curve includes exchange coupling between Co and the FM moment of C<sub>60</sub>.

Example Mumax3 script which produced Figure C.1 (red curve only).

```
Cz := 3e-9
setgridsize(128, 128, 2)
Setcellsize(2.5e-9, 2.5e-9, Cz)
Setgeom(Cuboid(3.2e-7, 3.2e-7, 6e-9))
ext_makegrains(12e-9, 100, 98473)
Defregion(100, layer(0))
Msat = 1400000
Afm := 3e-11
Aafm := 4e-12
Kfm := 2e4
Kafm := 2.7e7
Kspr := 5e5
amax := 100
for a:=0; a<amax; a++{
    anisU.setregion(a, vector(1+(0.1*randNorm()), 0.1*randNorm(), 0.1*randNorm()))
    Ku1.setregion(a, Kafm)
```

---

```
Aex.setregion(a, Aafm)
nodemagspins.setregion(a, 1}
anisU.setregion(100, vector(1, 0, 0))
Ku1.setregion(100, Kfm)
Aex.setregion(100, Afm)
m = uniform(1, 0, 0)
for b:=0; b<100; b++{
    ext_ScaleExchange(b, 100, 0.5)}
B_ext = vector(1500e-3, 0, 0)
Relax()
Bmax := 1500e-3
Bstep := 2e-4
MinimizerStop = 1e-6
TableAdd(B_ext)
TableAdd(CropLayer(m, 0))
TableAdd(CropLayer(m, 1))
for i:=Bmax; i>=-BmaX; i-=Bstep{
    B_ext = vector(i, 0, 0)
    minimize()
    tablesave()
    save(m)}
for b:=0; b<amax; b++{
    Ku1.setregion(b, Kspr)
    Aex.setregion(b, Afm)
    nodemagspins.setregion(b, 0)
    ext_scaleexchange(b, 100, 1)}
for i:=-Bmax; i<=BmaX; i+=Bstep{
    B_ext = vector(i, 0, 0)
    minimize()
    tablesave()
    save(m)}
for i:=Bmax; i>=-BmaX; i-=Bstep{
    B_ext = vector(i, 0, 0)
    minimize()
    tablesave()
    save(m)}
for i:=-Bmax; i<=BmaX; i+=Bstep{
    B_ext = vector(i, 0, 0)
    minimize()
    tablesave()
    save(m)}
```

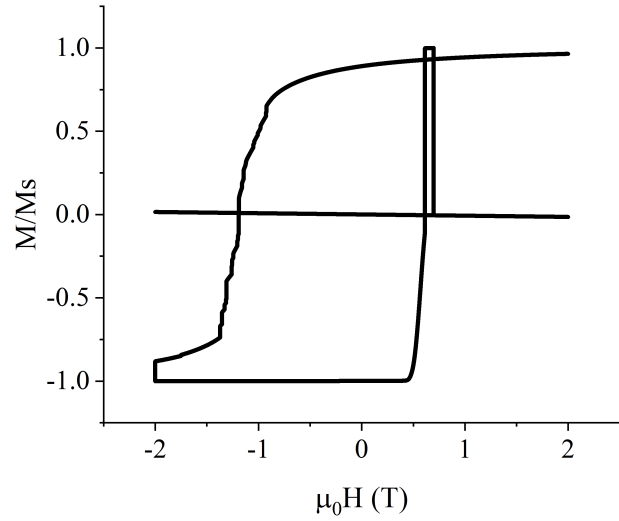


Figure C.2: Example of a failed simulation due to the use of a  $\beta$  release of Mumax3.

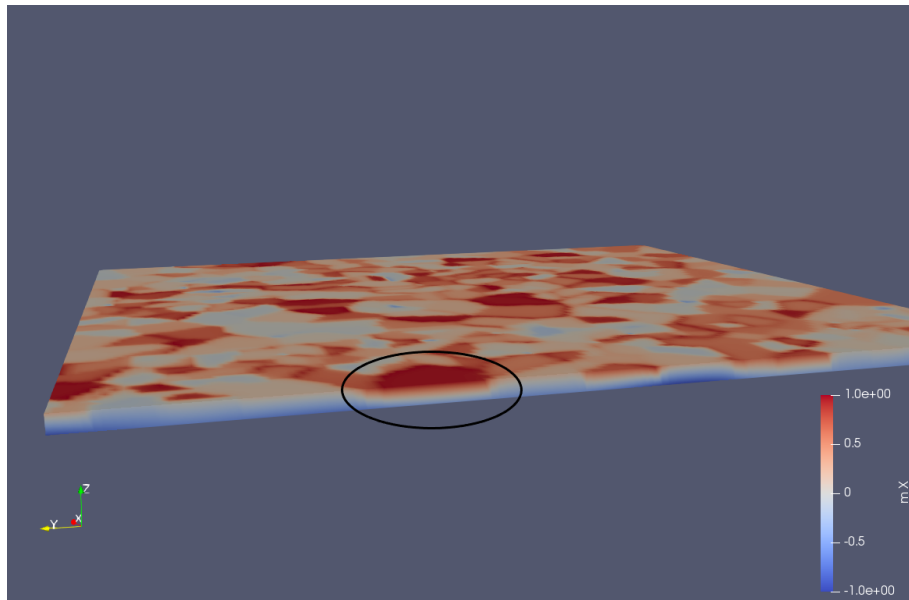


Figure C.3: Simulation box showing magnetisation of individual cells with the top layer as the AFM and bottom layer, the FM. Magnetic field applied is 0.219 (T) in the negative x direction. Blue represents cells aligned parallel with the field. Circled region highlights interfacial pinning producing a reduction in magnetisation in the form of rotation of magnetisation along the z-axis.

# REFERENCES

- [1] P. Desia, “Tesla’s electric motor shift to spur demand for rare earth neodymium — Reuters.”
- [2] M. Sagawa, S. Fujimura, N. Togawa, H. Yamamoto, and Y. Matsuura, “New material for permanent magnets on a base of Nd and Fe (invited),” *Journal of Applied Physics*, vol. 55, no. 6, pp. 2083–2087, 1984.
- [3] J. J. Croat, J. F. Herbst, R. W. Lee, and F. E. Pinkerton, “Pr-Fe and Nd-Fe-based materials: A new class of high-performance permanent magnets (invited),” *Journal of Applied Physics*, vol. 55, no. 6, pp. 2078–2082, 1984.
- [4] M. Ghezelbash, S. M. Darbani, A. E. Majd, and A. Ghasemi, “Temperature Dependence of Magnetic Hysteresis Loop of NdFeB with Uniaxial Anisotropy by LIBS Technique,” *Journal of Superconductivity and Novel Magnetism*, vol. 30, no. 7, pp. 1893–1898, 2017.
- [5] S. Trout, “Material selection of permanent magnets, considering thermal properties correctly,” in *Proceedings: Electrical Insulation Conference and Electrical Manufacturing and Coil Winding Conference (Cat. No.01CH37264)*, IEEE.
- [6] N. Moreley, “Introduction to Magnetism: Functional Properties,” 2018.
- [7] <https://tradingeconomics.com/commodity/neodymium>, “Neodymium market price 2012-2018.”
- [8] <https://uk.reuters.com/article/china-rareearths/china-cutting-rare-earth-output-unnerving-global-manufacturers-idUKL2N1WY1QR>, “China cutting rare earth output, unnerving global manufacturers.”

---

## REFERENCES

---

- [9] T. Dalgleish, J. M. G. Williams, A.-M. J. Golden, N. Perkins, L. F. Barrett, P. J. Barnard, C. Au Yeung, V. Murphy, R. Elward, K. Tchanturia, and E. Watkins, *Mineral Commodity Summaries*, vol. 136. 2018.
- [10] J. M. Klinger, *Rare Earth Frontiers: From Terrestrial Subsoils to Lunar Landscapes*. Cornell University Press, 2017.
- [11] T. Maughan, “The dystopian lake filled with the world’s tech lust,” 2015.
- [12] M. N. Baibich, J. M. Broto, A. Fert, N. Van Dau, and F. Petroff, “Giant Magnetoresistance of (001)Fe/(001)Cr Magnetic Superlattices,” *Physical Review Letters*, vol. 61, no. 21, pp. 2472–2475, 1988.
- [13] J. L. Leal and M. H. Kryder, “Spin valves exchange biased by Co/Ru/Co synthetic antiferromagnets,” *Journal of Applied Physics*, vol. 83, no. 7, pp. 3720–3723, 1998.
- [14] O. Gutfleisch, “Magnetic Materials for Energy Permanent Magnets Rare earth value chain Urban mine to,” 2013.
- [15] N. Minami, “Organic Solar Cells,” *Advanced Materials*, vol. 39, no. 12, pp. P458–P464, 1983.
- [16] T. Zyung, S. H. Kim, H. Y. Chu, J. H. Lee, S. C. Lim, J. I. Lee, and O. H. Jiyoung, “Flexible organic LED and organic thin-film transistor,” *Proceedings of the IEEE*, vol. 93, no. 7, pp. 1265–1272, 2005.
- [17] E. Cantatore, T. C. Geuns, G. H. Gelinck, E. Van Veenendaal, A. F. Gruijthuijsen, L. Schrijnemakers, S. Drews, and D. M. De Leeuw, “A 13.56-MHz RFID system based on organic transponders,” *IEEE Journal of Solid-State Circuits*, vol. 42, no. 1, pp. 84–92, 2007.
- [18] P.-m. Allemand, K. C. Khemani, A. Koch, F. Wudl, F. Wudl, K. Holczer, S. Donovan, G. Grtuner, J. O. E. D. Thompson, P.-m. Allemand, K. C. K. Ani, and A. Koch, “Organic Molecular Soft Ferromagnetism in a Fullerene C 60,” *Science*, vol. 253, no. 5017, pp. 301–303, 1991.
- [19] E. C. Stoner, “Collective Electron Ferromagnetism. II. Energy and Specific Heat,” *Proceedings of the Royal Society A: Mathematical, Physical and Engineering Sciences*, vol. 169, no. 938, pp. 339–371, 1939.

---

## REFERENCES

---

- [20] F.-S. Guo, R. M. Day, Y.-C. Chen, M.-L. Tong, A. Mansikkamaki, and R. A. Layfield, “Magnetic hysteresis up to 80 kelvin in a dysprosium metallocene single-molecule magnet,” *Science*, vol. 362, no. 6421, pp. 1400–1403, 2018.
- [21] F. Wudl and J. D. Thompson, “Buckminsterfullerene C60 and organic ferromagnetism,” *Journal of Physics and Chemistry of Solids*, vol. 53, no. 11, pp. 1449–1455, 1992.
- [22] J. Jo, J. Byun, I. Oh, J. Park, J. Mi-Jin, B.-C. Min, J. Lee, and J.-W. Yoo, “Molecular Tunability of Magnetic Exchange Bias and Asymmetrical Magneto-transport in Metalloporphyrin/Co Hybrid Bilayers,” *ACS Nano*, vol. 13, no. 1, pp. 894–903, 2018.
- [23] M. Gruber, F. Ibrahim, S. Boukari, L. Joly, V. Da Costa, M. Studniarek, M. Peter, H. Isshiki, H. Jabbar, V. Davesne, J. Arabski, E. Otero, F. Choueikani, K. Chen, P. Ohresser, W. Wulfhekel, F. Scheurer, E. Beaurepaire, M. Alouani, W. Weber, and M. Bowen, “Spin-dependent hybridization between molecule and metal at room temperature through interlayer exchange coupling,” *Nano Letters*, vol. 15, no. 12, pp. 7921–7926, 2015.
- [24] K. Bairagi, A. Bellec, V. Repain, C. Chacon, Y. Girard, Y. Garreau, J. Lagoute, S. Rousset, R. Breitwieser, Y. C. Hu, Y. C. Chao, W. W. Pai, D. Li, A. Smogunov, and C. Barreteau, “Tuning the Magnetic Anisotropy at a Molecule-Metal Interface,” *Physical Review Letters*, vol. 114, no. 24, p. 247203, 2015.
- [25] K. Harrison, “3DChem.”
- [26] <https://www.nobelprize.org/prizes/chemistry/1996/press-release>, “The 1996 Nobel Prize in Physics.”
- [27] P. C. Eklund, A. M. Rao, P. Zhou, Y. Wang, and J. M. Holden, “Photochemical transformation of C60 and C70 films,” *Thin Solid Films*, vol. 257, no. 2, pp. 185–203, 1995.
- [28] G. H. Kroll, P. J. Berming, Y. Chen, T. R. Ohno, J. H. Weaver, and R. E. Smalley, “Interaction of O<sub>2</sub> with C60: photon-induced oxidation,” *Chemical Physics Letters*, vol. 181, no. 2, 3, pp. 112–116, 1991.

---

## REFERENCES

---

- [29] J. M. Coey, “Permanent magnet applications,” *Journal of Magnetism and Magnetic Materials*, vol. 248, no. 3, pp. 441–456, 2002.
- [30] O. Céspedes, M. S. Ferreira, S. Sanvito, M. Kociak, and J. M. D. Coey, “Contact induced magnetism in carbon nanotubes,” *Journal of Physics Condensed Matter*, vol. 16, no. 10, pp. L155–L161, 2004.
- [31] T. Moorsom, M. Wheeler, T. Mohd Khan, F. Al Ma’Mari, C. Kinane, S. Langridge, D. Ciudad, A. Bedoya-Pinto, L. Hueso, G. Teobaldi, V. K. Lazarov, D. Gilks, G. Burnell, B. J. Hickey, and O. Cespedes, “Spin-polarized electron transfer in ferromagnet/C<sub>60</sub> interfaces,” *Physical Review B - Condensed Matter and Materials Physics*, vol. 90, no. 12, pp. 1–6, 2014.
- [32] T. Moorsom, *Electron transfer and spin injection in C<sub>60</sub>-ferromagnetic composites*. PhD thesis, 2016.
- [33] F. A. S. Al Ma’Mari, *Emergent Spin Ordering at C<sub>60</sub> interfaces*. PhD thesis, 2016.
- [34] G. Simon, *Manipulating the Magnetic Anisotropy of Cobalt with C<sub>60</sub> and the Effect of Annealing*. PhD thesis, 2017.
- [35] E. C. Stoner and E. P. Wohlfarth, “A mechanism of magnetic hysteresis in heterogeneous alloys,” *Philosophical Transactions of the Royal Society of London. Series A, Mathematical and Physical Sciences*, vol. 240, no. 826, pp. 599–642, 1948.
- [36] P. Fischer, T. Eimüller, G. Schütz, P. Guttmann, G. Schmahl, K. Pruegl, and G. Bayreuther, “Imaging of magnetic domains by transmission x-ray microscopy,” *Journal of Physics D: Applied Physics*, vol. 31, no. 6, pp. 649–655, 1998.
- [37] C. Tannous and J. Gieraltowski, “The Stoner-Wohlfarth model of ferromagnetism,” *European Journal of Physics*, vol. 29, no. 3, pp. 475–487, 2008.
- [38] J. Dubowik, “Shape anisotropy of magnetic heterostructures,” *Physical Review B - Condensed Matter and Materials Physics*, vol. 54, no. 2, pp. 1088–1091, 1996.
- [39] M. Rewienski, “Magnetic Surface Anisotropy in Ferromagnetic Thin Films with two rough surfaces,” *Acta Physica Polonica*, vol. 69, 1995.
- [40] R. L. White, “Physical boundaries to high-density magnetic recording,” *Journal of Magnetism and Magnetic Materials*, vol. 209, no. 1-3, pp. 1–5, 2000.

---

## REFERENCES

---

- [41] R. Hawig, E. F. K. Member, and R. Hawig, “The Exchange-Spring Magnet:,” *IEEE Transactions on Magnetics*, vol. 27, no. 4, pp. 3588–3600, 1991.
- [42] F. Wang, J. Zhang, J. Zhang, C. Wang, Z. Wang, H. Zeng, M. Zhang, and X. Xu, “Graded/soft/graded exchange-coupled thin films fabricated by [FePt/C]5/Fe/[C/FePt]5 multilayer deposition and post-annealing,” *Applied Surface Science*, vol. 271, pp. 390–393, 2013.
- [43] A. Bill and H. Braun, “Magnetic properties of exchange springs,” *Journal of Magnetism and Magnetic Materials*, vol. 272-276, pp. 1266–1267, 2004.
- [44] J. S. Jiang, S. D. Bader, H. Kaper, G. K. Leaf, R. D. Shull, A. J. Shapiro, V. S. Gornakov, V. I. Nikitenko, C. L. Platt, A. E. Berkowitz, S. David, and E. E. Fullerton, “Rotational hysteresis of exchange-spring magnets,” *Journal of Physics D: Applied Physics*, vol. 35, no. 19, pp. 2339–2343, 2002.
- [45] K. Son, *Tailored Magnetic Properties of Exchange-Spring and Ultra Hard Nanomagnets*. PhD thesis, 2017.
- [46] D. Suess, “Multilayer exchange spring media for magnetic recording,” *Applied Physics Letters*, vol. 89, no. 11, pp. 1–4, 2006.
- [47] D. Suess, M. Fuger, C. Abert, F. Bruckner, and C. Vogler, “Superior bit error rate and jitter due to improved switching field distribution in exchange spring magnetic recording media,” *Scientific Reports*, vol. 6, no. June, pp. 1–13, 2016.
- [48] W. H. Meiklejohn and C. P. Bean, “New Magnetic Anisotropy,” *Physical Review*, vol. 102, no. 5, pp. 1413–1414, 1956.
- [49] W. H. Meiklejohn and C. P. Bean, “New Magnetic Anisotropy,” *Physical Review*, vol. 105, no. 3, pp. 904–913, 1957.
- [50] J. Nogués, D. Lederman, T. J. Moran, and I. K. Schuller, “Positive Exchange Bias in Fe F2 -Fe Bilayers,” *Physical Review Letters*, vol. 76, no. 24, pp. 4624–4627, 1996.
- [51] J. Geshev, T. Dias, R. Julian, H. Liu, J. E. Schmidt, C. Van Haesendonck, K. Temst, A. Vantomme, and E. Menéndez, “Rotatable anisotropy driven training

---

## REFERENCES

---

- effects in exchange biased Co/CoO films,” *Journal of Applied Physics*, vol. 115, no. 24, p. 243903, 2014.
- [52] B. Dieny, V. S. Speriosu, S. S. P. Parkin, B. A. Gurney, D. R. Wilhoit, and D. Mauri, “Giant magnetoresistive in soft ferromagnetic multilayers,” *Physical Review B*, vol. 43, no. 1, pp. 1297–1300, 1991.
- [53] A. P. Malozemoff, “Mechanisms of exchange anisotropy,” *Journal of Applied Physics*, vol. 63, no. 8, pp. 3874–3879, 1988.
- [54] K. Zhang, T. Zhao, and H. Fujiwara, “Training effect of exchange biased iron–oxide/ferromagnet systems,” *Journal of Applied Physics*, vol. 89, no. 11, pp. 6910–6912, 2001.
- [55] J. Dean, A. Kovacs, A. Kohn, A. Goncharov, M. A. Bashir, G. Hrkac, D. A. Allwood, and T. Schrefl, “Exchange bias interactions in polycrystalline/amorphous bilayers,” *Applied Physics Letters*, vol. 96, no. 7, pp. 1–4, 2010.
- [56] M. Cadek, O. Vostrowsky, and A. Hirsch, “Carbon, 7. Fullerenes and Carbon Nanomaterials,” in *Ullmann’s Encyclopedia of Industrial Chemistry*, Weinheim, Germany: Wiley-VCH Verlag GmbH & Co. KGaA, 2010.
- [57] V. V. Diky and G. J. Kabo, “Thermodynamic properties of C 60 and C 70 fullerenes,” *Russian Chemical Reviews*, vol. 69, no. 2, pp. 95–104, 2002.
- [58] Agilent Technologies, “High and Ultra-High Vacuum for Science Research,” *Seminar on High and Ultra-High Vacuum for Science Research*, pp. 1–132, 2011.
- [59] C. Day, “Basics and Applications of Cryopumps,” *CERN Accelerator School Proceedings on ‘Vacuum in Accelerators’*, pp. 241–274, 2006.
- [60] F. Cataldo, “A Study on the Thermal Stability To 1000°C of Various Carbon Allotropes and Carbonaceous Matter Both Under Nitrogen and in Air,” *Fullerenes, Nanotubes and Carbon Nanostructures*, vol. 10, no. 4, pp. 293–311, 2002.
- [61] C. Pan, M. S. Chandrasekharaih, D. Agan, R. H. Hauge, and J. L. Marggrave, “Determination of sublimation pressures of a fullerene (C<sub>60</sub>/C<sub>70</sub>) solid solution,” *The Journal of Physical Chemistry*, vol. 96, no. 16, pp. 6752–6755, 2005.

## REFERENCES

---

- [62] C. S. Sundar, A. Bharathi, Y. Hariharan, J. Janaki, V. Sankara Sastry, and T. S. Radhakrishnan, “Thermal decomposition of C<sub>60</sub>,” *Solid State Communications*, vol. 84, no. 8, pp. 823–826, 1992.
- [63] E. A. Katz, D. Faiman, S. Shtutina, and A. Isakina, “Deposition and structural characterization of high quality textured C<sub>60</sub> thin films,” *Thin Solid Films*, vol. 368, no. 1, pp. 49–54, 2000.
- [64] R. J. Donnelly and C. F. Barenghi, “The Observed Properties of Liquid Helium at the Saturated Vapor Pressure,” *Journal of Physical and Chemical Reference Data*, vol. 27, no. 6, pp. 1217–1274, 1998.
- [65] P. T. Keyser and S. R. Jefferts, “Magnetic susceptibility of some materials used for apparatus construction (at 295 K),” *Review of Scientific Instruments*, vol. 60, no. 8, pp. 2711–2714, 1989.
- [66] J. M. Ngaruiya, S. Venkataraj, R. Drese, O. Kappertz, T. P. Leervad Pedersen, and M. Wuttig, “Preparation and characterization of tantalum oxide films produced by reactive DC magnetron sputtering,” *Physica Status Solidi (A) Applied Research*, vol. 198, no. 1, pp. 99–110, 2003.
- [67] R. Coloma Ribera, *Growth and thermal oxidation of Ru and ZrO<sub>2</sub> thin films as oxidation protective layers*. PhD thesis, 2017.
- [68] A. P. Mammana, I. L. Torriani, M. A. Silveira, and L. A. de Almeida, “Characterization of Ta thin films obtained by dc sputtering,” *Vacuum*, vol. 41, no. 4-6, pp. 1403–1404, 1990.
- [69] T. Campbell, R. K. Kalia, A. Nakano, P. Vashishta, S. Ogata, and S. Rodgers, “Dynamics of oxidation of aluminum nanoclusters using variable charge molecular-dynamics simulations on parallel computers,” *Physical Review Letters*, vol. 82, no. 24, pp. 4866–4869, 1999.
- [70] E. F. Kneller and F. E. Luborsky, “Particle size dependence of coercivity and remanence of single-domain particles,” *Journal of Applied Physics*, vol. 34, no. 3, pp. 656–658, 1963.

---

## REFERENCES

---

- [71] K. Maaz, M. Usman, S. Karim, A. Mumtaz, S. K. Hasanain, and M. F. Bertino, “Magnetic response of core-shell cobalt ferrite nanoparticles at low temperature,” *Journal of Applied Physics*, vol. 105, no. 11, 2009.
- [72] C. Nayek, K. Manna, G. Bhattacharjee, P. Murugavel, and I. Obaidat, “Investigating Size- and Temperature-Dependent Coercivity and Saturation Magnetization in PEG Coated Fe<sub>3</sub>O<sub>4</sub> Nanoparticles,” *Magnetochemistry*, vol. 3, no. 2, p. 19, 2017.
- [73] I. M. Obaidat, B. Issa, B. A. Albiss, and Y. Haik, “Temperature Dependence of Saturation Magnetization and Coercivity in Mn 0.5 Zn 0.5 Gd 0.02 Fe 1.98 O 4 Ferrite Nanoparticles ,” *IOP Conference Series: Materials Science and Engineering*, vol. 92, p. 012012, 2015.
- [74] M. Ali, C. H. Marrows, M. Al-Jawad, B. J. Hickey, A. Misra, U. Nowak, and K. D. Usadel, “Antiferromagnetic layer thickness dependence of the IrMn/Co exchange-bias system,” *Physical Review B - Condensed Matter and Materials Physics*, vol. 68, no. 21, pp. 1–7, 2003.
- [75] F. Radu and H. Zabel, “Exchange bias effect of ferro-/antiferromagnetic heterostructures,” *Springer Tracts in Modern Physics*, vol. 227, pp. 97–184, 2007.
- [76] T. Moorsom and O. Cespedes, “Magnetic pinning at metal-organic interfaces,” 2018. Condensed Matter Forum.
- [77] J. Nogues and I. K. Schuller, “Exchange Bias,” *Magnetism and Magnetic Materials*, vol. 192, no. 2, pp. 203–232, 1999.
- [78] M. C. Hickey and J. S. Moodera, “Origin of intrinsic Gilbert damping,” *Physical Review Letters*, vol. 102, no. 13, 2009.
- [79] A. Vansteenkiste, J. Leliaert, M. Dvornik, M. Helsen, F. Garcia-Sanchez, and B. Van Waeyenberge, “The design and verification of MuMax3,” *AIP Advances*, vol. 4, no. 10, pp. 1–32, 2014.
- [80] J. M. Coey, “Permanent magnets: Plugging the gap,” *Scripta Materialia*, vol. 67, no. 6, pp. 524–529, 2012.

---

## REFERENCES

---

- [81] J. De Clercq, A. Vansteenkiste, M. Abes, K. Temst, and B. Van Waeyenberge, “Modelling exchange bias with MuMax3,” *Journal of Physics D: Applied Physics*, vol. 49, no. 43, 2016.
- [82] A. Harres and J. Geshev, “A polycrystalline model for magnetic exchange bias,” *Journal of Physics Condensed Matter*, vol. 24, no. 32, 2012.
- [83] J. De Clercq, J. Leliaert, and B. Van Waeyenberge, “Modelling compensated antiferromagnetic interfaces with MuMax3,” *Journal of Physics D: Applied Physics*, vol. 50, no. 42, 2017.
- [84] M. Zakotnik and C. O. Tudor, “Commercial-scale recycling of NdFeB-type magnets with grain boundary modification yields products with ’designer properties’ that exceed those of starting materials,” *Waste Management*, vol. 44, pp. 48–54, 2015.
- [85] J. M. Coey, *Magnetism and Magnetic Materials*. Cambridge University Press, 3rd ed., 2009.
- [86] S. C. Wang and Y. Li, “In situ TEM study of Nd-rich phase in NdFeB magnet,” *Journal of Magnetism and Magnetic Materials*, vol. 285, no. 1-2, pp. 177–182, 2005.
- [87] A. Enders, R. Skomski, and J. Honolka, “Magnetic surface nanostructures,” *Journal of Physics Condensed Matter*, vol. 22, no. 43, 2010.
- [88] J. P. Prieto-Ruiz, F. M. Romero, H. Prima-García, and E. Coronado, “Exchange coupling in an electrodeposited magnetic bilayer of Prussian blue analogues,” *Journal of Materials Chemistry C*, vol. 3, no. 42, pp. 11122–11128, 2015.
- [89] J. P. Rueff, R. M. Galera, C. Giorgetti, E. Dartige, C. Brouder, and M. Alouani, “Rare earth contributions to the X-ray magnetic circular dichroism at the Co K edge in rare earth-cobalt compounds investigated by multiple-scattering calculations,” *Physical Review B - Condensed Matter and Materials Physics*, vol. 58, no. 18, 1998.
- [90] K. Raghavachari and C. M. Rohlffing, “Structures and vibrational frequencies of carbon molecules (C<sub>60</sub>, C<sub>70</sub>, and C<sub>84</sub>),” *The Journal of Physical Chemistry*, vol. 95, no. 15, pp. 5768–5773, 2005.